JFM PAPERS

Investigations on the turbulent/non-turbulent interface in supersonic compressible plate turbulent boundary layer

Shuhuai Su[1], Yanguang Long[1], Jinjun Wang[1],† and Xinliang Li[2]

[1]Fluid Mechanics Key Laboratory of Education Ministry, Beihang University, Beijing 100191, PR China

[2]LHD, Institute of Mechanics, Chinese Academy of Sciences, Beijing 100190, PR China

The turbulent boundary layer (TBL) is a widely existing flow phenomenon in nature and engineering applications. Its strong mixing effect can achieve more sufficient material mixing, heat transport, etc. The understanding of the entrainment process and mechanism of irrotational fluids entering the turbulent region can be promoted by studying the geometric and dynamic characteristics of turbulent/non-turbulent interfaces (TNTI). In compressible flow, it is unclear whether the properties of TNTI will change and whether the entrainment will show different features due to the influence of compressibility. Based on the direct numerical simulation results of supersonic compressible plate TBLs with Mach number of 2.9, the geometric and dynamic characteristics of TNTI are investigated in this paper. The interface is identified by the enstrophy method, and the height, thickness, fractal dimension, enstrophy transportation and entrainment characteristics of the interface are investigated. It is found that for the enstrophy transportation in a TBL, the contribution of compressibility-related terms accounts for approximately 13.4 % of the total enstrophy transportation, which tends to transfer the enstrophy of turbulence near the interface to both directions vertical to the interface. This promotes the expansion of the turbulent region towards the non-turbulent region, and the mean height, thickness and entrainment velocity are increased by approximately 3.7 %, 7.0 % and 8.5 %, respectively, while the fractal dimension is basically unaffected. Different from the incompressible flow, the contribution of the compressibility-related terms to the entrainment velocity is independent of the local curvature, and the intense entrainment process is more likely to occur on a highly curved concave surface.

Key words: turbulent boundary layers, compressible turbulence, compressible boundary layers

† Email address for correspondence: jjwang@buaa.edu.cn

1. Introduction

In order to study the mixing between the turbulent boundary layer (TBL) and free flow, it is necessary to determine the interface between them in the instantaneous flow, also known as the turbulent/non-turbulent interface (TNTI). Physically, TNTI refers to a twisted thin layer that separates instantaneous turbulent and non-turbulent regions. It was shown in previous studies (Wolf *et al.* 2013; Philip *et al.* 2015; Long, Wang & Pan 2022) that the geometric features of TNTI are closely related to the entrainment process of irrotational fluid entering the turbulent region in the incompressible TBL, jet, shear flow and wake. Further investigations on the geometric and dynamic properties of TNTI are needed to reveal the different mechanisms involved in the entrainment and their interaction effects. In compressible flow, whether the characteristics of TNTI will change and whether the entrainment will show different features due to the influence of compressibility also need further exploration. Therefore, it is of great significance and application to explore the TNTI features of compressible flow.

Accurately identifying the TNTI in the flow is a necessary prerequisite for discussing interface characteristics. With the development of flow visualization technics various mature interface detection methods have been developed. The current mainstream interface detection methods distinguish turbulent and non-turbulent regions through a given threshold of a characteristic physical scalar. The mostly used scalar is the enstrophy ($\Omega = \omega_i \omega_i$) (Borrell & Jimenez 2016) due to the rotational nature of turbulence. In addition for flow which is dominated by spanwise shear flow such as TBL, Natrajan & Christensen (2006) found that using spanwise vorticity (ω_z) as the scalar is basically consistent with the results using the enstrophy under the appropriate threshold condition. da Silva *et al.* (2014) pointed out that the volume fraction of the turbulent zone identified by the vorticity monotonically decreases with the increase of threshold. However, within a certain range there exists a platform where the volume fraction of the turbulent zone remains almost unchanged as the threshold changes, which means that the values within the platform can serve as thresholds for the detection.

Scalar fields were used to identify the interface (Prasad & Sreenivasan 1989; Gampert *et al.* 2014; Watanabe *et al.* 2015). It was found that at appropriate thresholds, the interfaces identified by the scalar field method and the enstrophy method were almost identical (Gampert *et al.* 2014). Watanabe *et al.* (2015) further pointed out that the condition to ensure that the interface identified by the scalar field method and the enstrophy method is consistent is that the flow has a unified Schmidt number.

In order to reduce the interference of noise in the flow data measured in the experiment, Chauhan *et al.* (2014) proposed an interface detection method based on turbulent kinetic energy. However, Watanabe, Zhang & Nagata (2018) noted that the interface detected by the turbulent kinetic energy method may be physically different from the other one. Eisma, Westerweel & Ooms (2015) assumed that the interface identified by the turbulent kinetic energy method is actually the upper surface of the uniform momentum zone (UMZ) farthest from the wall, rather than the TNTI.

A time-averaged detection method based on virtual particle tracking was further proposed (Long, Wu & Wang 2021), which broadcasts virtual particles in the flow and tracks their velocity fluctuation as the scalar to identify the interface. The virtual particle tracking method can effectively identify the small-scale structures of the interface and has good robustness, which can adapt well to interface research in noisy flow and high free stream turbulence conditions.

The geometric properties of the TNTI in incompressible flow, such as the height, thickness and fractal dimension of the interface, have been fully studied. Wu *et al.* (2020)

used the turbulent kinetic energy method to count the position of TNTI in the TBL of a grooved wall and a smooth wall, and pointed out that in the TBL of the smooth wall the mean height of the TNTI is $Y_i = 0.82\delta_{99}$, the root-mean-square (r.m.s.) of the height is $\sigma_i = 0.16\delta_{99}$. Here δ_{99} represents the thickness of boundary layer defined as the height from the wall where the average streamwise velocity reaches 99 % of the incoming velocity, and the probability density function (p.d.f.) of the height is basically in agreement with the normal distribution.

Although the TNTI is defined mathematically as the equivalent surface of the scalar, in practice, it should have a certain thickness. Aguirre & Catrakis (2020) used the reciprocal of the vertical gradient of the scalar to quantify the interface thickness, analysed the far field of the circular jet with Reynolds number $Re \sim 20\,000$ and Schmidt number $Sc \sim 2000$, and the interface thickness was visualized. It was found that the thickness continuously changes throughout the entire interface. Zhang, Watanabe & Nagata (2018b) computed the conditional mean profiles of the vorticity and its derivative with respective to local coordination. Further, 15 % of the peak value of the derivative was chosen as the boundary to define the mean thickness of the TNTI, and the thickness of the viscous superlayer (VSL) and the turbulent sublayer (TSL) inside the interface was further divided through the relationship between the production term and the viscous diffusion term in the enstrophy transport equation. It was found that as the Reynolds number increases, the thickness of the interface and the VSL remain almost unchanged, approximately 15η and $4\text{--}5\eta$, respectively, where η is defined as the Kolmogorov scale in the turbulence (Zhang, Watanabe & Nagata 2023).

Based on interface detection results, the geometric structures of the TNTI have received great attention. Lee, Sung & Zaki (2017) and Mistry, Philip & Dawson (2019) found that there are large-scale fluctuations in the TNTI overall while small wrinkle structures form the local geometric shapes. These two kinds of structures are, respectively, believed to be related to large-scale motions and instantaneous entrainment processes on the TNTI. The multiscale structures of the TNTI indicate that the interface may have fractal characteristic. de Silva *et al.* (2013) tried to use fractal dimension to describe the multiscale features of the TNTI. Fractal dimension is generally used to describe the complexity of the interface, and can be computed by the box-counting method, that is, for a two-dimensional image, boxes with different side lengths r are used to divide it, and the minimum number of boxes required to cover the image N_b is counted. Within a certain range, the following relationship exists:

$$N_b \propto r^{-D}, \tag{1.1}$$

where D is the fractal dimension. It was found that in the TBL, the two-dimensional fractal dimension is approximately 1.3, and when extrapolated to the three-dimensional situation, the fractal dimension is approximately 2.3. Borrell & Jimenez (2016) further investigated the TBL with various Reynolds numbers through numerical simulation, and discovered that the fractal dimension of the TNTI is related to the threshold selection, and the result of de Silva corresponds to the case that the threshold is 1 in the work.

Entrainment is the process of the turbulent region expanding into the non-turbulent region, which can be divided into engulfment and nibbling according to the mechanism. Engulfment is mainly manifested by the deformation of the large-scale structures of the interface, which carries part of the irrotational fluid into the turbulent region, forming irrotational bubbles. At the same time, some turbulent fluid will also enter the potential flow region, forming drops (da Silva *et al.* 2014; Jahanbakhshi & Madnia 2016; Wu *et al.* 2020). Nibbling is mainly manifested as the irrotational fluid undergoes viscous

diffusion at the interface to obtain vorticity and transform into turbulence (Holzner & Lüthi 2011; Mistry *et al.* 2019). Engulfment was considered as the dominant mechanism of entrainment in early studies (Dahm & Dimotakis 1987; Ferré *et al.* 1990; Mungal, Karasso & Lozano 1991; Dimotakis 2000). However, it has recently been figured out that nibbling may be the main influencing factor. Mathew & Basu (2002) pointed out that in turbulent jets, the volume of the engulfed fluid is much smaller than the volume of the turbulent region, indicating that the entrainment is mainly dominated by the nibbling. Holzner & Lüthi (2011) proposed a method to calculate the entrainment velocity using the enstrophy transport equation. It was observed that the magnitude of the local entrainment velocity is consistent with the Kolmogorov velocity magnitude, which seems to imply that the viscous diffusion at the VSL is the main driving force for the outward expansion of turbulence. At present, it is believed by the main researchers (Chauhan *et al.* 2014; da Silva *et al.* 2014; Borrell & Jimenez 2016) that engulfment and nibbling contribute to the expansion of turbulent region in different aspects: the conversion of laminar fluid to turbulence requires the contribution from viscosity, and the differences in expansion velocity of different types of turbulence are related to the strength of engulfment.

The geometric properties of the TNTI are closely related to the entrainment. It has been found that the interface is mainly composed of surfaces with a curvature radius of approximately Taylor microscale, and the entrainment process mainly occurs through the highly concave surface. Specifically, the local entrainment velocity is correlated with the local curvature of the interface. A higher interfacial entrainment velocity can be observed on highly curved concave surfaces, indicating that there is a greater tendency for the intense entrainment process (Wolf *et al.* 2012, 2013; Philip *et al.* 2015).

It has been shown above that interface entrainment is related to geometric features mainly influenced by small-scale structures such as local interface curvature. However, there is a lack of research on the impact of large-scale structures on entrainment. Long *et al.* (2022) quantitatively analysed the impact of instantaneous large-scale motions on the entrainment near the interface, and discovered that the engulfment is enhanced near high-speed motions (H-SM), and local nibbling is weakened, while the opposite is true at low-speed motions (L-SM); At the same time, the tortuosity of the interface near the H-SM increases, while the interface near the L-SM becomes flatter. This is more outstanding than the variation in entrainment velocity, which leads to a distinct increase in entrainment flux near the H-SM and a decrease near the L-SM.

In the field of compressible flow, Jahanbakhshi & Madnia (2016) quantitatively studied the geometric features and entrainment process of the TNTI in compressible turbulence at different Mach numbers, and noted that in the entrainment the contribution of the compressibility-related terms is small. As the Mach number increases, the entrainment mass flux gradually decreases. It was assumed that the entrainment mainly occurs through the concave region on the TNTI. As the Mach number increases, the proportion of concave regions on the interface decreases from 64 % to 59 %, with the proportion of elliptical concave regions decreasing from 36 % to 32 %, and the proportion of convex regions increasing from 36 % to 41 %. This change in interface geometry leads to a decrease in the entrainment mass flux. However, neither the reason why compressibility changes the geometric shapes of the interface nor the role of compressibility in enstrophy transport process has been explained.

In this paper, the direct numerical simulation (DNS) results of supersonic compressible plate TBL with Mach number of 2.9 are analysed, and the influence of compressibility on the geometric features and entrainment characteristics of the TNTI is studied. Section 2 of the paper introduces the simulation parameters and basic characteristics of the

flow of the DNS data used in this article, to ensure that the DNS results can meet the analysis of the TNTI characteristics. Section 3 is the analysis of the geometric features of the TNTI, including height, thickness and fractal characteristics. Section 4 presents the entrainment characteristics of TNTI, including enstrophy transportation and entrainment characteristics. Finally, § 5 will try to give a potential conclusion on the role of compressibility in the process of entrainment.

2. Basic characteristics of the flow

2.1. *Simulation parameters*

The DNS is conducted for supersonic compressible flat TBL at Mach 2.9. The length of the entire flow is 431.49 mm (streamwise x) $\times$ 35 mm (transverse y) $\times$ 14 mm (spanwise z), and the grid size is $3100 \times 360 \times 375$. Here Re_θ and Re_τ at $Re_x = 2.0 \times 10^6$ are 4118 and 1270, respectively, while at the outlet of the flow are 5581 and 1359 while the Reynolds number Re_x is 5581.4 mm^{-1}. The pressure of the inlet is $p_\infty = 2296$ Pa. The ratio of boundary layer thickness to the height of the simulation area at the beginning of the fully TBL (coordinate $x = -40$ mm) and the outlet is 0.2611 and 0.3006, respectively. The spatial resolution $\Delta x^+ = 9.20$, $\Delta z^+ = 5.52$, $\Delta y^+ = 0.552$, which reaches the viscous scale and can accurately resolve turbulent dissipation. The time step is 0.005 normalized time scale, which is defined as 1 mm$/U_\infty \approx 1.65 \times 10^{-6}$ s, and the sampling frequency is 5 normalized time scale to track a total of 200 DNS flow fields from normalized time scale 5 to 1000.

An isothermal boundary condition with $T_w/T_\infty = 1.25$ has been applied to the wall, and a laminar velocity profile is set at the inlet. Sponge layer and non-reflective boundary conditions are used at the outlet and upper boundary. The scheme WENO_SYMBO_LMT, which uses a seventh-order weighted essentially non-oscillatory scheme (Martín *et al.* 2006), is used for the inviscid terms, while an eighth-order central scheme and three-step third-order Runge–Kutta method are applied for the viscous terms and time progression, respectively. A bypass transition mode is adopted and achieved by introducing blowing and suction disturbances, which has been introduced by Pirozzoli, Grasso & Gatski (2004).

The settings of simulation parameters are similar to the plate TBL in the compression ramp of Dang *et al.* (2022) and Duan *et al.* (2021). Figure 1(*a–c*) are given to show the instantaneous streamwise velocity, temperature and density fields. It can be seen that the flow rapidly transforms into turbulence. The diagonal lines extending from the inlet in temperature and density fields are caused by the disturbances to accelerate the transition instead of leading-edge shock.

2.2. *Time-averaged properties*

Figure 2 shows the streamwise variation of boundary layer thickness and shape factor. Boundary layer thickness is defined as the height from the corresponding position to the wall where the mean streamwise velocity reaches 99 % of the incoming velocity. The horizontal axis is Reynolds number, which is defined as

$$Re_x = \rho \frac{U_\infty x}{\mu} = \frac{U_\infty x}{\nu}. \tag{2.1}$$

The streamwise variation of boundary layer thickness is marked by the blue line with diamonds, which shows that the boundary layer gradually thickens along the
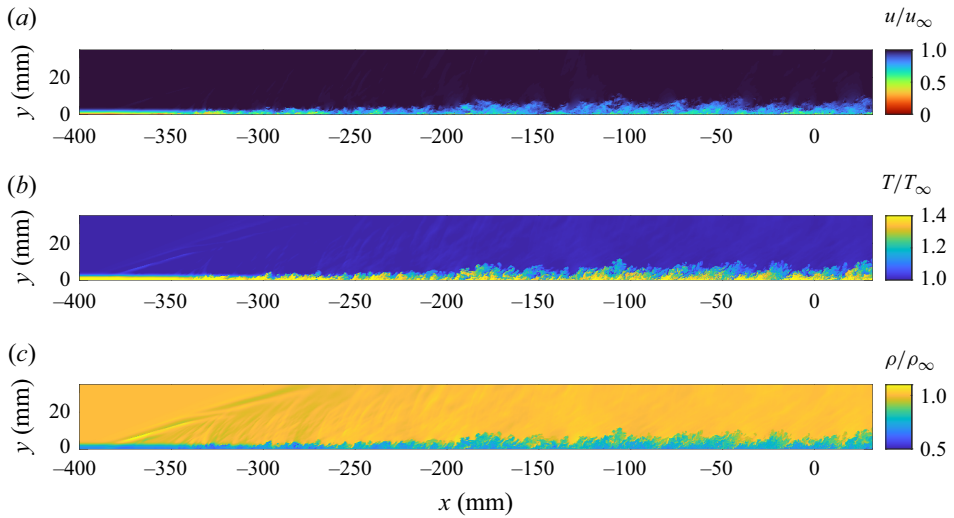
Figure 1. Instantaneous streamwise velocity, temperature and density fields. (*a*) Streamwise velocity field normalized by incoming velocity. (*b*) Temperature field normalized by incoming flow temperature. (*c*) Density field normalized by incoming flow density.
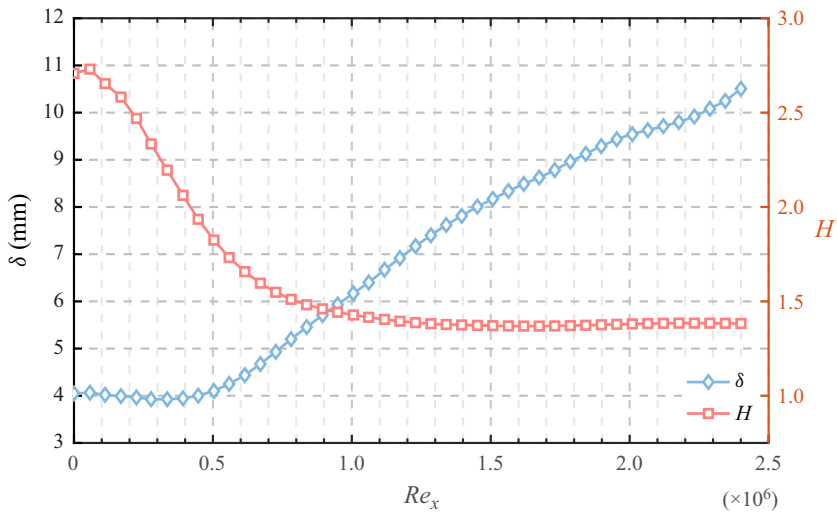

Figure 2. The streamwise variation of thickness and shape factor of the boundary layer: blue line with diamonds for thickness and red line with squares for shape factor.

streamwise direction. At the inlet of the flat plate, the boundary layer has a short thinning trend, this is because the flow is driven by pressure, and the boundary layer is affected by the barotropic gradient at the inlet. The shape factor H is defined as the ratio of displacement thickness δ to momentum loss thickness θ (2.2), which is marked by a brown curve with circles in the figure,

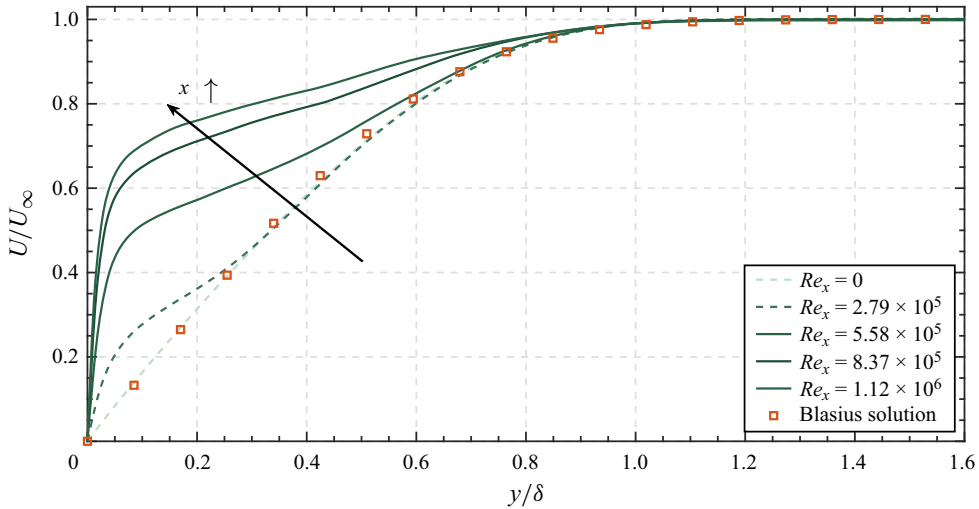$$H = \frac{\delta}{\theta}. \tag{2.2}$$

Figure 3. Mean profiles of streamwise velocity at different streamwise positions of the developing region.

At the inlet of the flat plate, the shape factor H is approximately 2.6, indicating that the flow is laminar. As the flow develops, it gradually decreases and tends to the minimum stable value of 1.4, and the corresponding $Re_x \approx 1.0 \times 10^6$, indicating that the flow has reached the fully developed TBL. The change in shape factor preliminarily indicates the process of flow transition from laminar to turbulence. Typical mean profiles of streamwise velocity at different streamwise positions of the developing region are shown in figure 3. The velocity is normalized by the incoming flow velocity, and the height from the wall is normalized by the local boundary layer thickness. Different types of green curves are the distributions of the time-averaged streamwise velocity at different locations in the developing region of the flow, and the grid data are the velocity distribution of the standard Blasius solution. At the inflow, the streamwise velocity is in good agreement with the Blasius solution, which indicates that the flow is laminar. As the flow develops, the time-averaged profile of the streamwise velocity gradually becomes full, indicating the occurrence of the transition.

Figure 4 shows the mean profile of streamwise velocity of the turbulent region. The velocity and the height from the wall are normalized by the wall friction velocity. The wall friction velocity can be obtained as

$$u_\tau = \sqrt{\frac{\tau_w}{\rho_w}}, \tag{2.3}$$

where τ_w is defined as

$$\tau_w = \rho_w \nu_w \left(\frac{\mathrm{d}U}{\mathrm{d}y} \right)_{y=0}. \tag{2.4}$$

The mean profile of streamwise velocity shows linear growth in the near-wall region and logarithmic growth in the slightly far-wall region. These two regions are called linear region and logarithmic region, respectively, where the logarithmic region can be fitted by

$$U^+ = \frac{1}{\kappa} \ln y^+ + B. \tag{2.5}$$
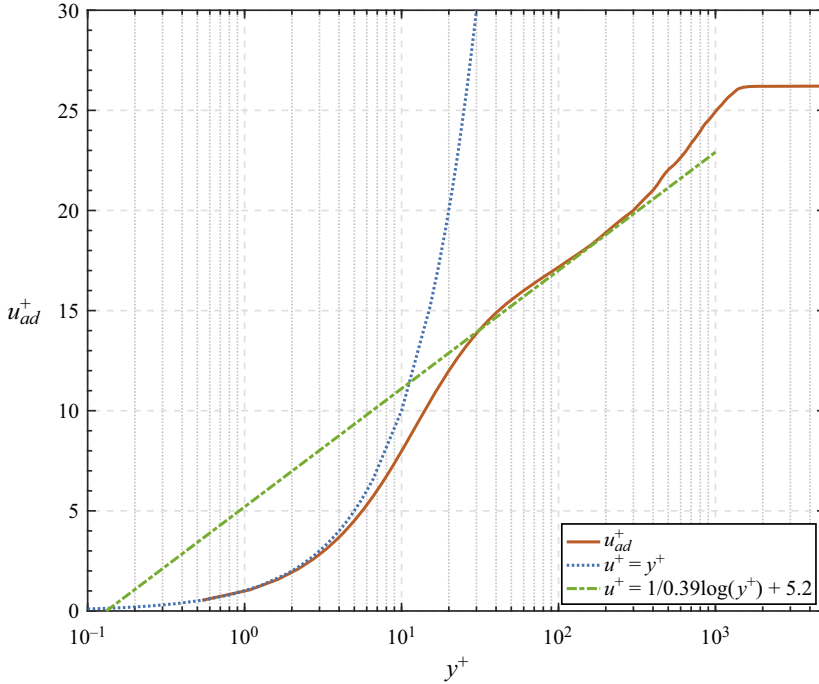
988 A30-7

Figure 4. Mean profile of streamwise velocity of turbulent region corrected by van Driest transformation at $Re_x = 2.29 \times 10^6$.

For the supersonic compressible TBL, if the logarithmic region fitting is performed directly, the parameters will be different from the classical profile, and then van Driest transformation is required (Van Driest 1951; Duan, Beekman & Martín 2011). The van Driest transformation uses density as the parameter to modify the mean profile of streamwise velocity of compressible flow, as follows:

$$\mathrm{d}u_{vd}^+ = \sqrt{\frac{\bar{\rho}}{\bar{\rho}_w}}\mathrm{d}U^+, \quad y^+ = y\frac{u_\tau}{\bar{\nu}_w}, \tag{2.6a,b}$$

where $\bar{\rho}$ is the Reynolds averaged mean density at the corresponding y coordinate, $\bar{\rho}_w$ is the average density at the wall and u_{vd}^+ is the mean profile of streamwise velocity corrected by the van Driest method. After correction, the logarithmic region is in good agreement with the classical profile, with $\kappa = 0.39$ and $B = 5.2$ in this paper.

2.3. *Statistical characteristics*

The streamwise variation of the skin friction coefficient is plotted in figure 5 to find the position where the flow becomes fully turbulent. Since the skin friction of compressible flow is a function of Mach number, Reynolds number and the wall temperature, it is necessary to transform the compressible value into an incompressible value. A method with temperature values correction has been applied (Qian 2004), the reference temperature is decided as follows:

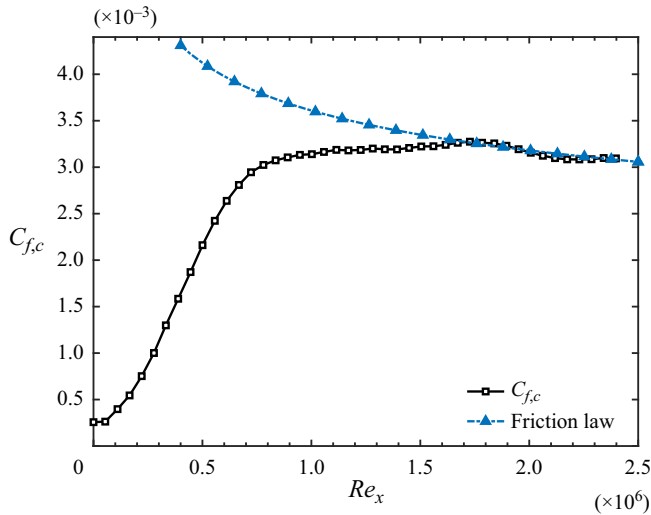$$T^* = T_\infty + 0.5(T_w - T_\infty) + 0.22(T_r - T_\infty). \tag{2.7}$$

Figure 5. The streamwise variation of skin friction coefficient.

The corresponding relationship between μ and T can be calculated as

$$\frac{\mu^*}{\mu_\infty} = \left(\frac{T^*}{T_\infty}\right)^\omega. \tag{2.8}$$

In the present work, ω has been decided as 0.76. Then the relationship between compressible and incompressible skin friction can be obtained as follows, where $C_{f,c}$ represents the compressible value and $C_{f,i}$ represents the incompressible value:

$$C_{f,c} = C_{f,i}\left(\frac{T^*}{T_\infty}\right)^{-((4-\omega)/5)} = C_{f,i}\left(\frac{T^*}{T_\infty}\right)^{-0.648}, \quad (\omega = 0.76). \tag{2.9}$$

It can be seen that at $Re_x = 1.8 \times 10^6$ the skin friction coefficient reaches the maximum value and then begins to decay. The friction law with Re_x has been given as $C_f = 0.370$ $(\log_{10} Re_x)^{-2.584}$ (Schlichting & Gersten 2017) and has been plotted with the blue line, which can be seen to be fitted well with the present results after $Re_x = 1.8 \times 10^6$. Combined with the result of the shape factor, the flow after $Re_x = 1.8 \times 10^6$ can be considered to have become fully TBL.

The r.m.s. profiles of fluctuating velocity at different streamwise positions of the turbulent region are shown in figures 6(*a*) and 6(*b*). In figure 6(*a*) the height from the wall and the r.m.s. profiles of fluctuating velocity is normalized by the wall friction velocity, which is called inner scale normalization. In figure 6(*b*) the wall height and r.m.s. velocity are normalized by semilocal scale y^*, which is defined as

$$y^* = y/\delta_v^*, \quad \delta_v^* = \bar{\mu}/\bar{\rho}u_\tau^*, \quad u_\tau^* = \sqrt{\frac{\tau_w}{\bar{\rho}}}, \tag{2.10a–c}$$

where $\bar{\mu}, \bar{\rho}$ are Reynolds-averaged mean dynamic viscosity μ and Reynolds-averaged mean density ρ. In the range of $Re_x = 1.12 \times 10^6$–1.57×10^6, the r.m.s. profiles of fluctuating velocity hardly change with the streamwise positions of flow with the peak positions around $y^+ = y^* \approx 10$–20. Figures 6(*c*) and 6(*d*) further analyse the distribution
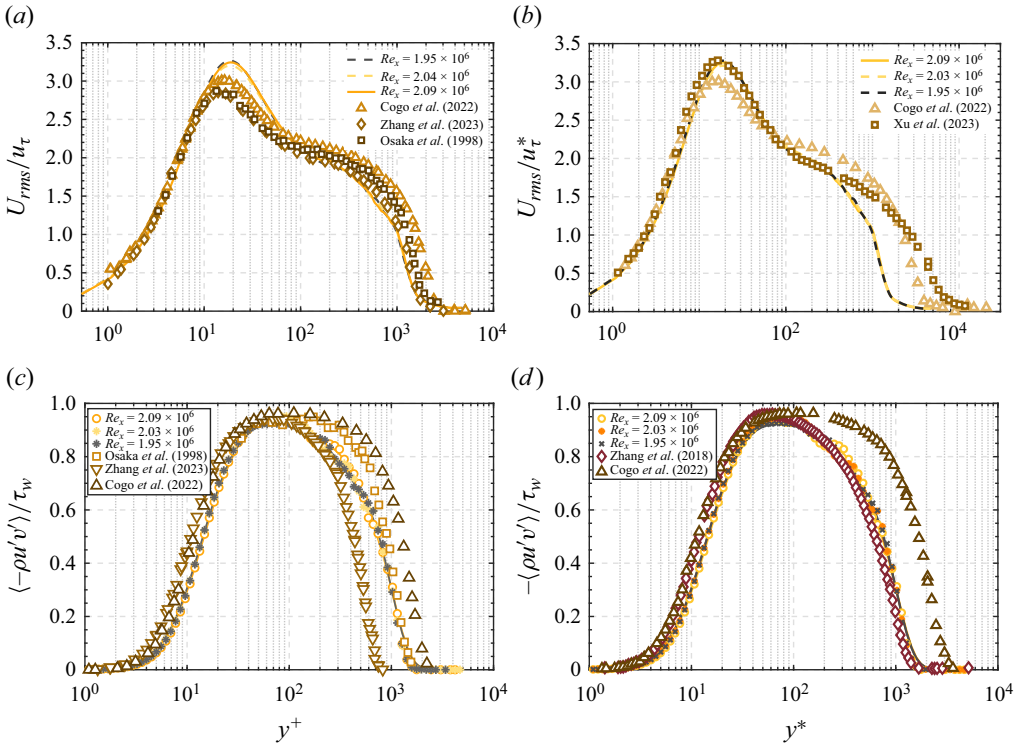
Figure 6. Normalized r.m.s. velocity and Reynolds stress at different positions compared with previous results. Inner scale y^+ is used in (a,c) while semilocal scale y^* is used in (b,d).

of Reynolds stress at different streamwise positions in the turbulent region, and it can be seen that the distribution of Reynolds stress at different positions is also in good agreement. The results are compared with some previous works (Osaka, Kameda & Mochizuki 1998; Zhang, Duan & Choudhari 2018a; Cogo *et al.* 2022; Xu, Wang & Chen 2023; Zhang *et al.* 2023). It can be seen that in figure 6(*a*) the present work is fitted well with previous results, while in figure 6(*b*) there are some differences above $y^* \approx 10^2$. This might be caused by the difference in Re_θ and Re_τ (Cogo *et al.* (2022) at $Re_\tau = 1947$ and Xu *et al.* (2023) at $Re_\tau = 2282$). The same situation occurs in figure 6(*c*) (Osaka *et al.* (1998) at $Re_\theta = 5040$, Cogo *et al.* (2022) at $Re_\theta = 7562$ and Zhang *et al.* (2023) at $Re_\theta = 2206$) and figure 6(*d*) (Zhang *et al.* (2018a) at $Re_\theta = 2835$). For the sake of conservatism, the flow within the range $Re_x = 1.80 \times 10^6$–2.4×10^6 is considered to have completely developed into TBL. This paper will focus on the geometric features and entrainment characteristics of the TNTI in the TBL region.

In order to prevent the narrow spanwise simulation domain from affecting the calculation results, it is necessary to determine the spanwise gradient of the streamwise velocity. Figure 7 shows the mean profile of the spanwise gradient of the streamwise velocity at $Re_x = 2.0 \times 10^6$. It can be seen that $\overline{\partial(u/u_\infty)/\partial z}$ remains smaller than 1 % with small jitter caused by calculation errors, which means the gradient would not affect the simulation results.

The turbulent Mach number is plotted against y^+ to investigate the distribution of the compressibility along the transverse. Turbulent Mach number M_T can be
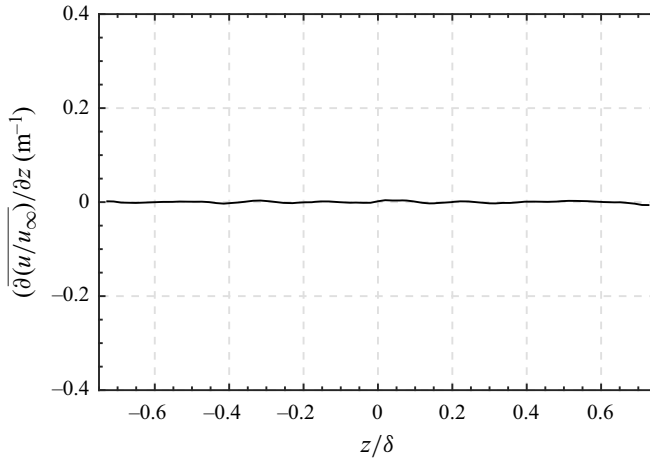
Figure 7. Mean profile of spanwise gradient of the streamwise velocity at $Re_x = 2.0 \times 10^6$.
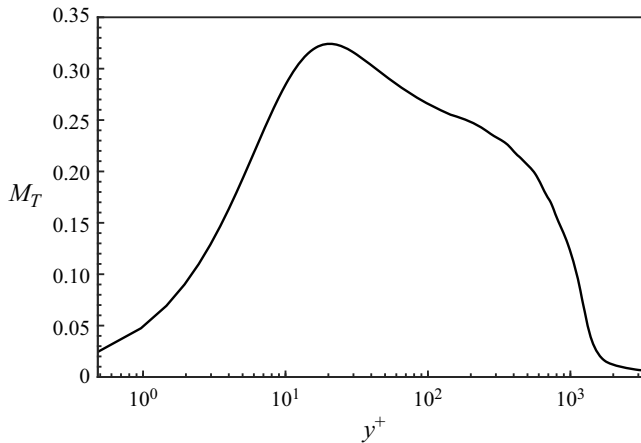

Figure 8. The mean profile of turbulent Mach number at $Re_x = 2.29 \times 10^6$.

defined as

$$M_T = \frac{\overline{(u'_i u'_i)}^{1/2}}{\bar{c}}, \quad c = \sqrt{\gamma \frac{R_0}{\tilde{M}} T}, \tag{2.11a,b}$$

where $\bar{c}$ is the average local speed of sound, R_0 is the universal gas constant and $\tilde{M}$ is the molar mass of gas. It can be seen in figure 8 that the peak value is approximately 0.32, which means that the compressibility can have a certain effect on the flow and the turbulent structures.

3. Interface geometric features

3.1. *Height of the interface*

In order to investigate the geometric features of the TNTI, it is necessary to accurately identify the interface. The distribution characteristic of enstrophy is used to determine the threshold of the scalar in this paper. The p.d.f. of enstrophy in the region
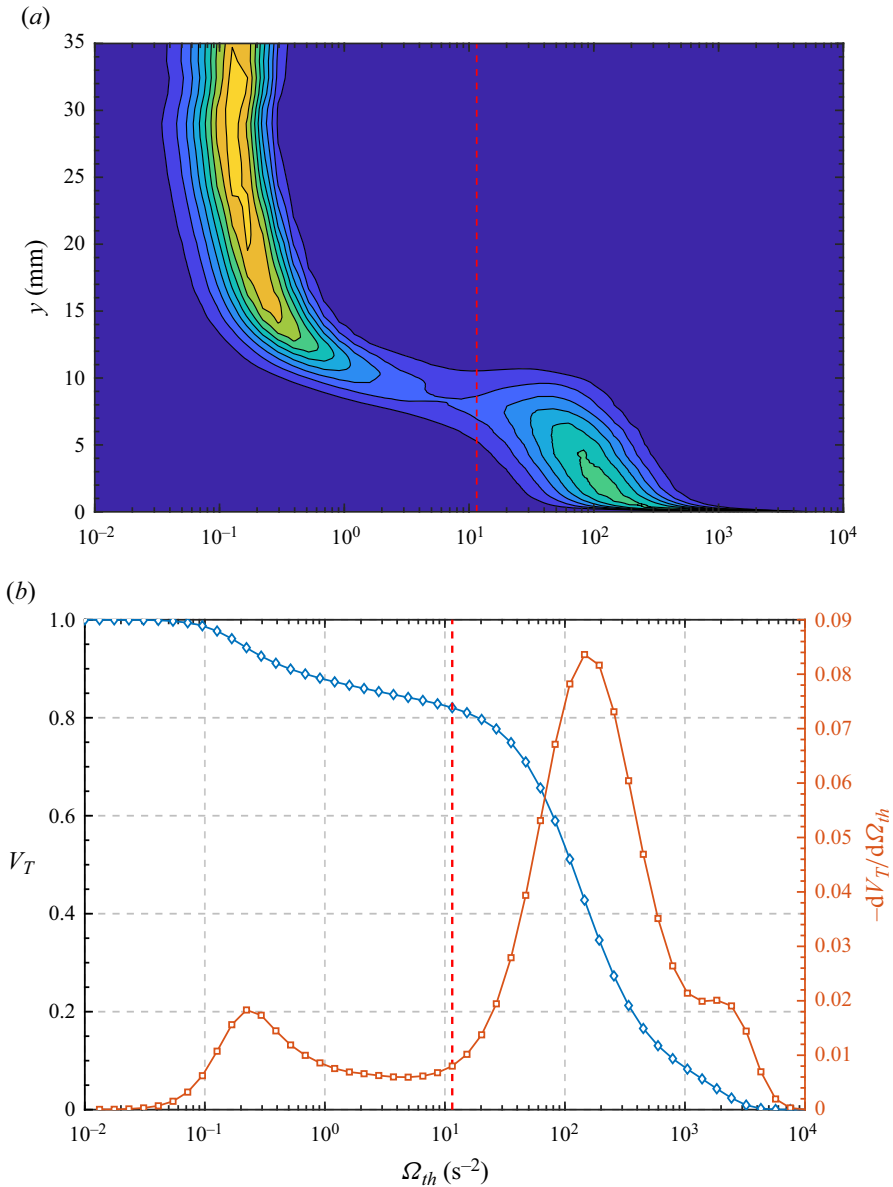
(*a*)

(*b*)

Figure 9. Threshold selection. (*a*) Probability density distribution of enstrophy. (*b*) Volume fractions and the first derivative of it plotted against threshold selection.

$Re_x = 1.95 \times 10^6$–2.23×10^6 has been shown in figure 9(*a*) as an example of threshold selection. It can be seen that there are high enstrophy areas near the wall and low enstrophy areas far from the wall. The threshold used is selected on the connection area, with the amount of 11.514 marked by the red dotted line. Figure 9(*b*) shows the volume fractions and their first derivative with respective to threshold selection. It can be seen that there is a platform area near the threshold selected, indicating that the volume of the turbulent zone is not sensitive to threshold selection within this range.
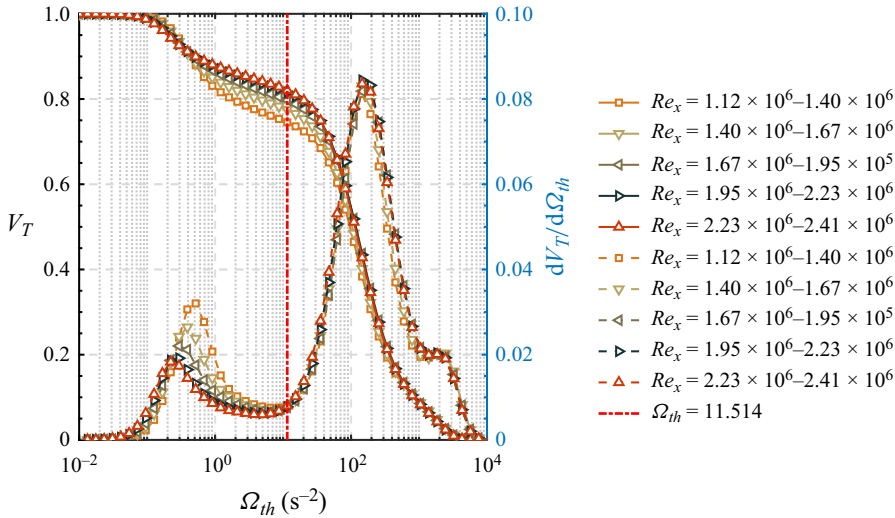
988 A30-12

Figure 10. Volume fractions and the first derivative of it plotted against threshold selection at different positions. Solid lines represent the volume fractions while dash lines are used to represent the first derivative.

To ensure that the threshold used for detection does not change at different positions in the turbulent region, figure 10 shows the volume fractions of the turbulent region and its first derivative with respective to the threshold selection at different streamwise positions. The dashed line represents the first derivative of the volume fractions, while the solid line represents the volume fractions. Although the profiles of derivatives at different positions do not completely match, the platform areas are generally the same. Therefore, in the TBL region, the same threshold can be used for interface detection, with the threshold 11.514 marked by the red dashed line.

The enstrophy method and a recognition method defined by the UMZ method are used to identify the interface to make a comparison. The UMZ method uses the square of momentum defect M_{def} as the scalar (Cogo *et al.* 2022). In this paper, the scalar M_{def} and its threshold are defined as

$$M_{def} = \frac{(\rho u - \rho_\infty u_\infty)^2 + (\rho v - \rho_\infty v_\infty)^2 + (\rho w - \rho_\infty w_\infty)^2}{(\rho_\infty u_\infty)^2} = 0.001. \qquad (3.1)$$

The instantaneous enstrophy contour plot and the instantaneous TNTI recognized by the enstrophy method and UMZ method are shown in figure 11. It can be seen that though these two TNTIs are similar, the TNTI identified by the UMZ method does not match well with the outer edge of the enstrophy field. The interface is so smooth that it can be considered as having some small-scale information erased from it. In contrast, the small wrinkle structures of the TNTI recognized by the enstrophy method match well with the outer edge of the enstrophy field, indicating that the enstrophy method effectively recognizes multiscale features on the TNTI, which is beneficial for subsequent analysis. The TNTI identified by the enstrophy method within the area between $Re_x = 1.95 \times 10^6$–2.41×10^6 has been used to investigate the properties of the TNTI.

The geometric features of the interface are closely related to the entrainment, and the height of the TNTI is discussed in the paper. The mean value and r.m.s. value of the interface height at different streamwise positions are shown in figure 12. At the inlet of flat plate, the flow state is laminar, and the height of the interface Y_i is equivalent
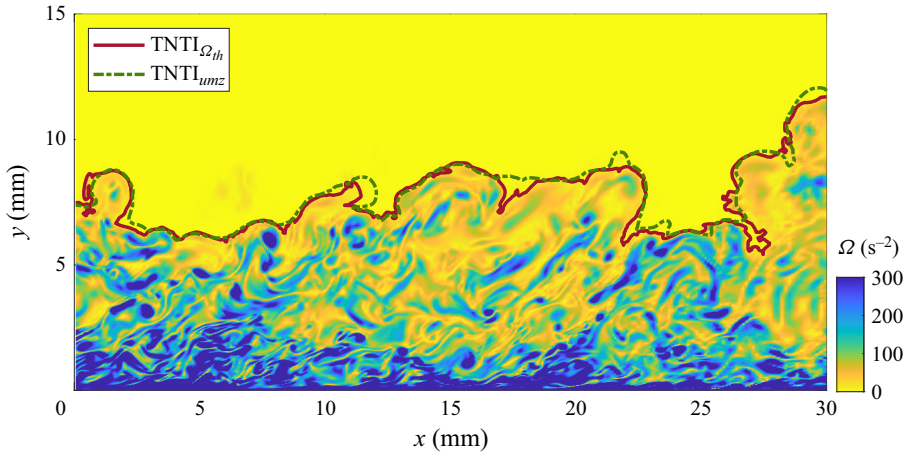
Figure 11. Instantaneous enstrophy contour plot and instantaneous TNTI recognized by enstrophy method and UMZ method.
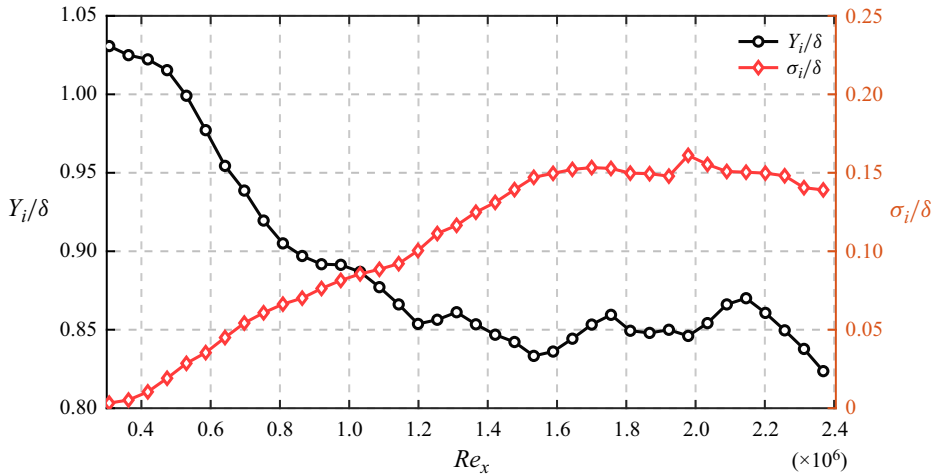

Figure 12. Streamwise variation of mean and r.m.s. interface height.

to the thickness of the boundary layer. As the flow gradually develops into turbulence the Y_i/δ rapidly decreases and the normalized r.m.s. σ_i/δ gradually increases, indicating that the outer edge of the boundary layer is becoming more and more intermittent with the transition. In the turbulent region, Y_i/δ and σ_i/δ tend to stabilize at 0.85 and 0.15, respectively. The comparison between this result and the results of incompressible TBL in some previous works (Corrsin & Kistler 1995; Wu *et al.* 2020) is shown in table 1. It can be seen that when the Mach number is 2.9, compressibility tends to increase the mean height of the interface. In this paper the mean height is increased by 3.7 %. The mechanism will be explored in § 4.

3.2. *Interface thickness and fractal characteristics*

The conditional average profiles of enstrophy are used in this article to obtain the interface thickness. An interface coordinate system is established to get conditional average profiles

Conditions	Re_τ	$skew_i$	Y_i/δ	σ_i/δ
Corrsin & Kistler (1995)	<2000	0	0.83	0.16
Wu *et al.* (2020) smooth plate	483	0	0.82	0.16
Present work	1359	0	0.85	0.15

Table 1. Comparison of mean and r.m.s. height with previous works.
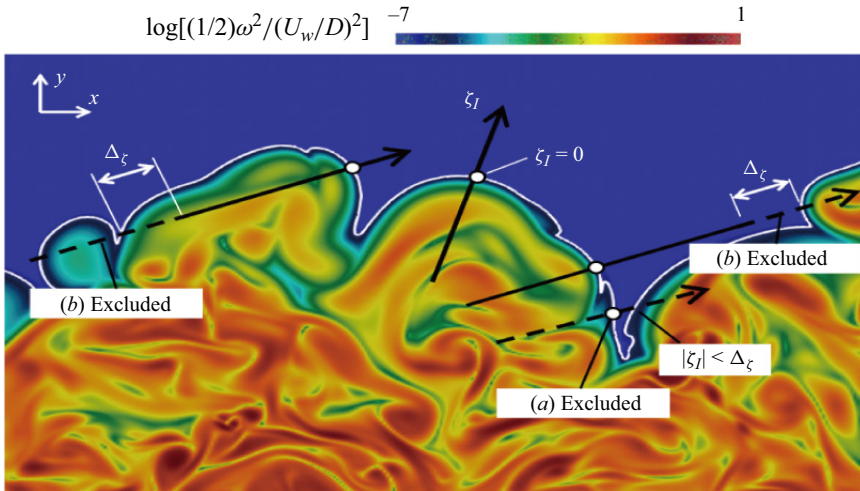

Figure 13. Establishment of interface coordinate axis (Watanabe *et al.* 2018).

(Watanabe *et al.* 2018). As shown in figure 13, the vertical axis of the interface coordinate is perpendicular to the interface. A small difference between the coordinate established in this article and figure 13 is that the vertical axis does not point to the non-turbulent region but points to the turbulent region. This means that when the vertical axis y_I is positive, it is located inside the turbulent zone. Here y_I ranges from -95η to 95η and is discretized by 100 points. The flow at the height of 0.5δ is used as the reference layer to calculate the Kolmogorov scale η. For the case where the coordinate passes through the interface multiple times, the area within 10 points away from the interface will be ignored, as shown by the dashed line in figure 13.

Figure 14 shows the conditional mean profile of enstrophy within the range $Re_x = 1.28 \times 10^6$–1.46×10^6, where the black curve represents the enstrophy, and the red dashed line represents the derivative with respective to the interface coordinate y_I. The interface thickness δ_i is calculated based on the interval between the position where the derivative reaches 20 % of the peak value and the position where the interface coordinate y_I is 0 (Zhang *et al.* 2018b), as shown in the shaded part of the figure. The interface thickness is approximately 16.8η. This change in average thickness may be caused by the increase of *Ma* and Reynolds number. The comparison of interface thickness with previous results by Zhang *et al.* (2018b, 2023) is shown in figure 15. It has been found that as the Re_θ increases, the mean thickness of the TNTI remains almost unchanged within approximately 15.7η (Zhang *et al.* 2023) while the increase of *Ma* has a significant effect on the thickness (Zhang *et al.* 2018b) with limited data. This shows that the compressibility may tend to increase the mean thickness of the interface. In this paper the thickness is increased by
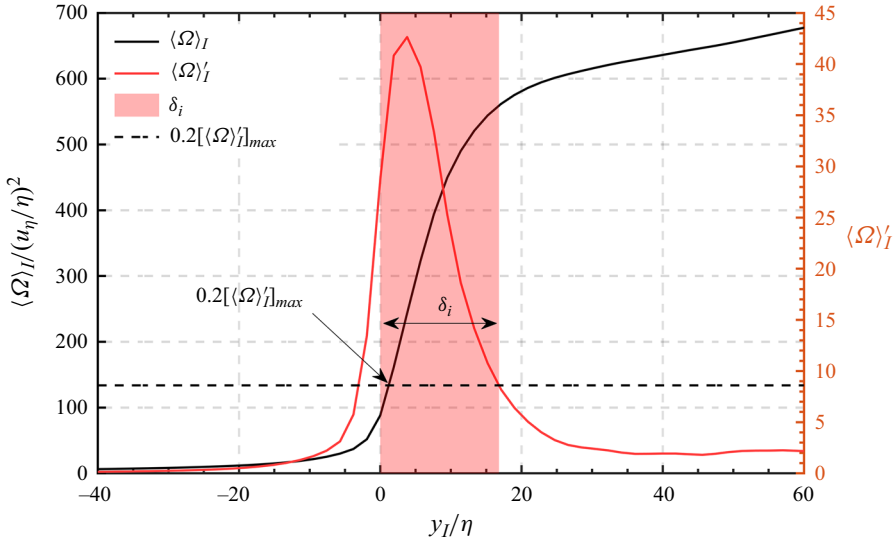
Figure 14. Conditioned mean profile of enstrophy field and its derivative with respective to interface coordinate y_I.
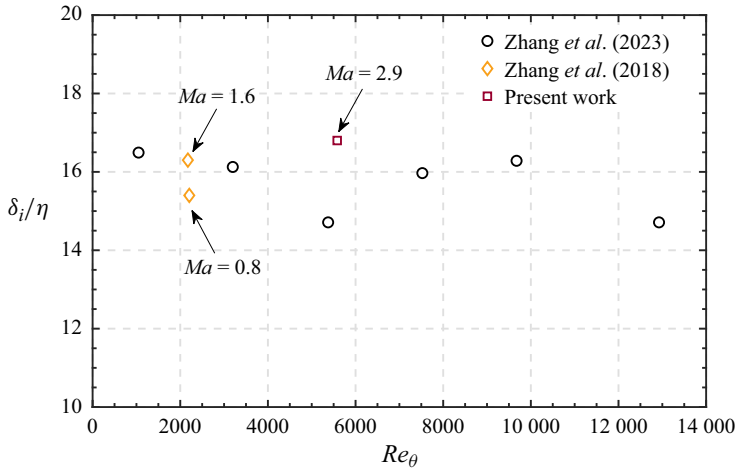

Figure 15. Comparison of interface thickness with the works by Zhang *et al.* (2018*b*, 2023).

approximately 7.0 %. A potential mechanism related to compressibility will be explained in § 4, however, more data is needed to reveal it.

The fractal dimension is used to describe the fractal characteristics of the interface, and the box-counting method is used to analyse the interface in the range of $Re_x = 0-2.79 \times 10^5$, $2.79 \times 10^5-5.58 \times 10^5$, $5.58 \times 10^5-8.37 \times 10^5$, $8.37 \times 10^5-1.12 \times 10^6$, $1.12 \times 10^6-1.40 \times 10^6$, $1.40 \times 10^6-1.67 \times 10^6$, $1.67 \times 10^6-1.95 \times 10^6$, $1.95 \times 10^6-2.23 \times 10^6$. The box size range is $0.01\delta-\delta$. The corresponding relationship between N_b and r in the range of $Re_x = 1.95 \times 10^6-2.23 \times 10^6$ is shown in figure 16(*a*). The blue circle represents the number of boxes corresponding to different box sizes, and the red solid line represents the fitting result. The slope of the fitted line
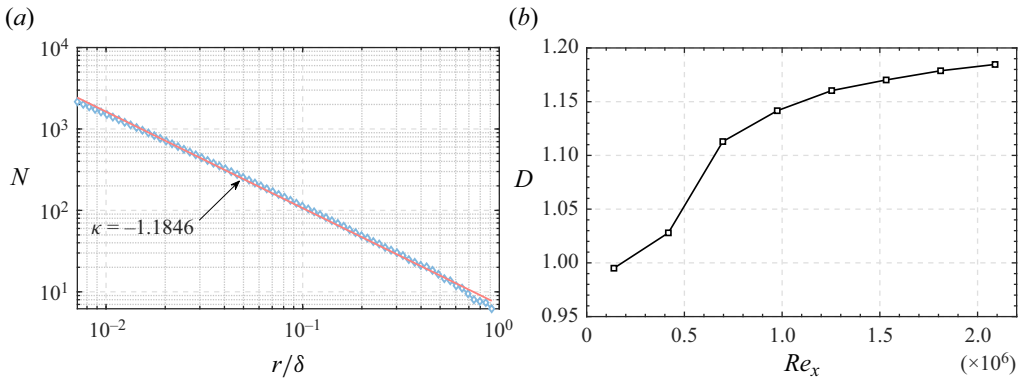
Figure 16. The fractal characteristic of TNTI. (*a*) Interface fractal dimension in the range of $Re_x = 1.95 \times 10^6$–2.23×10^6. (*b*) The streamwise variation of fractal dimension.
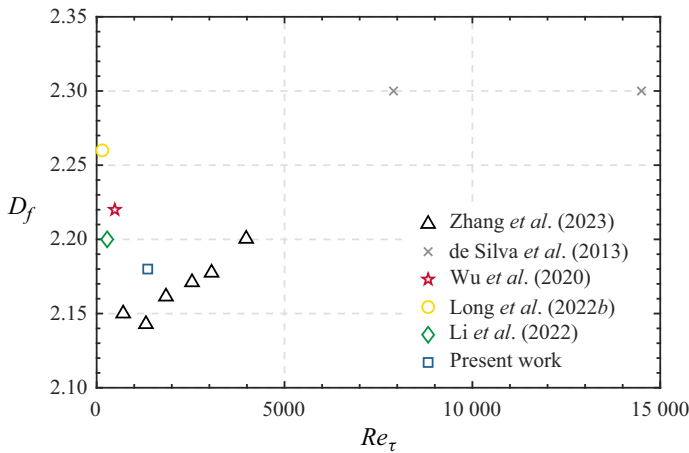

Figure 17. Comparison of fractal dimension results between present work and previous works.

is approximately -1.18. According to (1.1), the fractal dimension D is approximately 1.18 and D_f is approximately 2.18, which is slightly smaller than the previous result of incompressible TBL with $D_f = 2.3$ (de Silva *et al.* 2013). This may be related to the small Reynolds number and Mach number of the flow, rather than the influence of compressibility. The comparison of fractal dimension results between the present work and some previous works is shown in figure 17, which indicates that the fractal dimensions are affected by the Reynolds number and D_f may get closer to 2.3 at a higher Reynolds number (Zhang *et al.* 2023) while the *Ma*-dependency of D_f still lacks investigation. However, the fractal dimension in a compressible supersonic TBL with $Ma = 2.83$ and $Re_\theta = 9.14 \times 10^4$ has been investigated (Zhuang *et al.* 2018) and it was found that the D_f is 2.31, which is consistent with the results of high Reynolds number. This may indicate that the Mach number has little effect on the fractal dimension, but further research is still needed to support it. Figure 16(*b*) shows the streamwise variation of the fractal dimension. It can be seen that the fractal dimension of the interface gradually increases, which indicates that with the development of the flow, the intermittency of the boundary layer increases, and the TNTI also becomes more distorted. In the turbulent region, the

fractal dimension gradually approaches approximately 1.18 in this investigation. As the flow further develops, D_f may increase further.

4. Interface entrainment characteristics

Entrainment is the process of irrotational fluids entering the turbulent region, and currently, the velocity v_n of the fluids relative to the TNTI is generally defined as the entrainment velocity. Mathematically, the TNTI can be defined as the equivalent surface of enstrophy, where the following relationship exists:

$$\frac{\mathrm{D}^s \Omega}{\mathrm{D}^s t} = \frac{\partial \Omega}{\partial t} + U_j^s \frac{\partial \Omega}{\partial x_j} = 0, \tag{4.1}$$

where D^s represents the material derivative of fluid elements at the TNTI, U_j^s is the velocity of the fluid elements at the interface. Due to the fact that the velocity of the fluid elements can be decomposed into the velocity of the TNTI motion (U_j) and the velocity of the relative TNTI motion (V_j), (4.1) can be rewritten as follows:

$$\frac{\mathrm{D}^s \Omega}{\mathrm{D}^s t} = \frac{\partial \Omega}{\partial t} + (U_j + V_j) \frac{\partial \Omega}{\partial x_j} = 0. \tag{4.2}$$

The V_j here is the entrainment velocity v_n. When v_n is negative, it represents the process of irrotational flow entering the turbulent region. Moving it to the right-hand side of the equation we can get the formula as

$$\left(\frac{\partial \Omega}{\partial t} + U_j \frac{\partial \Omega}{\partial x_j} \right) = \frac{\mathrm{D}\Omega}{\mathrm{D}t} = -v_n \frac{\partial \Omega}{\partial x_j} = -v_n |\nabla \Omega|. \tag{4.3}$$

Equation (4.3) indicates that the local entrainment velocity at the interface is completely determined by the material derivative of the enstrophy divided by the absolute value of the enstrophy gradient. The material derivative of enstrophy can be obtained from the enstrophy transport equation. In incompressible flow, the enstrophy transport equation is as follows:

$$\frac{\mathrm{D}\Omega}{\mathrm{D}t} = 2\omega_i \omega_j S_{ij} + 2\nu \omega_i \nabla^2 \omega_i. \tag{4.4}$$

In (4.4), S_{ij} is the local strain rate tensor

$$S_{ij} = \frac{1}{2} \left(\frac{\partial u_i}{\partial x_j} + \frac{\partial u_j}{\partial x_i} \right). \tag{4.5}$$

The first term on the right-hand side of (4.4) represents the increase in enstrophy caused by the stretching/compression of vortex, which is called the production term. The second term is the viscous term, which can be further written as the sum of the viscous diffusion term and the viscous dissipation term,

$$2\nu \omega_i \nabla^2 \omega_i = \nu \nabla \cdot (\nabla \Omega) - 2\nu \nabla \omega_i : \nabla \omega_i. \tag{4.6}$$

By substituting (4.4), (4.5) and (4.6) into (4.3), the entrainment velocity in incompressible flow can be obtained as

$$v_n = \frac{-2\omega_i \omega_j S_{ij}}{|\nabla \Omega|} - \frac{\nu \nabla (\nabla \Omega)}{|\nabla \Omega|} + \frac{2\nu \nabla \omega_i : \nabla \omega_i}{|\nabla \Omega|}. \tag{4.7}$$

Equation (4.7) shows that in incompressible flow, the entrainment velocity is affected by three terms: the production of enstrophy; viscous diffusion; viscous dissipation. In

988 A30-18

compressible flow, the enstrophy transport equation is as follows:

$$\frac{\mathrm{D}\Omega}{\mathrm{D}t} = 2\omega_i\omega_j\frac{\partial u_i}{\partial x_j} - 2\Omega\frac{\partial u_j}{\partial x_j} + \frac{2\omega_i\epsilon_{ijk}}{\rho^2}\frac{\partial \rho}{\partial x_j}\frac{\partial p}{\partial x_k} + \nu\frac{\partial^2\Omega}{\partial x_j\partial x_j}$$

$$- 2\nu\frac{\partial \omega_i}{\partial x_j}\frac{\partial \omega_i}{\partial x_j} - \frac{2\omega_i\epsilon_{ijk}}{\rho^2}\frac{\partial \rho}{\partial x_j}\frac{\partial \tau_{km}}{\partial x_m}. \tag{4.8}$$

Comparing (4.8) with (4.4), the compressible form of the enstrophy transport equation has additional components: the component generated by fluid expansion/compression (the second term on the right-hand side of the equation), namely the dilatation term; the component generated by the baroclinic torque caused by the misalignment of density and pressure gradients (the third term on the right-hand side of the equation), namely the baroclinic term; the component caused by the torque generated by the variation of the shear stress in the density gradient field (the sixth term on the right-hand side of the equation), namely the density gradient term. These three terms can quantitatively analyse the effect of compressibility on the enstrophy transportation, and further analyse its effect on the entrainment velocity. For ease of description, Ω_I–Ω_{VI} will be used in the subsequent section of this paper to represent the production term, dilatation term, baroclinic term, viscous diffusion term, viscous dissipation term and density gradient term from left to right on the right-hand side of (4.8), respectively, and $\mathrm{D}\Omega/\mathrm{D}t$ will be used to represent the total enstrophy transportation.

4.1. *Enstrophy transport characteristics*

The conditional mean profiles of the production term, viscous diffusion term and viscous dissipation term on both sides of the interface are shown in figure 18: the blue solid line represents the production term, the green dotted line represents the viscous diffusion term and the red dashed line represents the viscous dissipation term. These three terms are roughly of the same order of magnitude near the interface. The conditional mean profiles of the compressibility independent terms are basically consistent with those in the incompressible TBL (Watanabe *et al.* 2018; Zhang *et al.* 2018*b*; Long *et al.* 2022).

The conditional mean profiles of Ω_I–Ω_{VI} and $\mathrm{D}\Omega/\mathrm{D}t$ are shown in figure 19, where the black dashed line represents the total enstrophy transportation. The production term, viscous dissipation term and viscous diffusion term have a large magnitude near the interface, indicating that these three terms play a dominant role in the entrainment. However, the dilatation term, baroclinic term and density gradient term caused by compressibility have a smaller order of magnitude, which is shown as a straight line near zero in the figure.

In order to further investigate the influence of compressibility on the enstrophy transportation, figure 20(*a*) compares the conditional mean profiles of the contribution of compressibility independent terms and the total enstrophy transportation. It can be spotted that the two are in good agreement in most areas, and $\mathrm{D}\Omega/\mathrm{D}t$ has a certain change compared with the contribution of compressibility independent terms in the entire interface thickness. The changes near the interface are magnified in figure 20(*a*), which shows that $\mathrm{D}\Omega/\mathrm{D}t$ is decreased due to the compressibility-related terms near the interface especially at the interface coordinate $y_I = 1.9\eta$ (the red line). The proportion of compressibility-related terms in the total enstrophy transportation at different locations in the interface coordinate is shown in figure 20(*b*), which proves the conclusion above. The proportion gradually decreased from approximately 2 % outside the interface, began
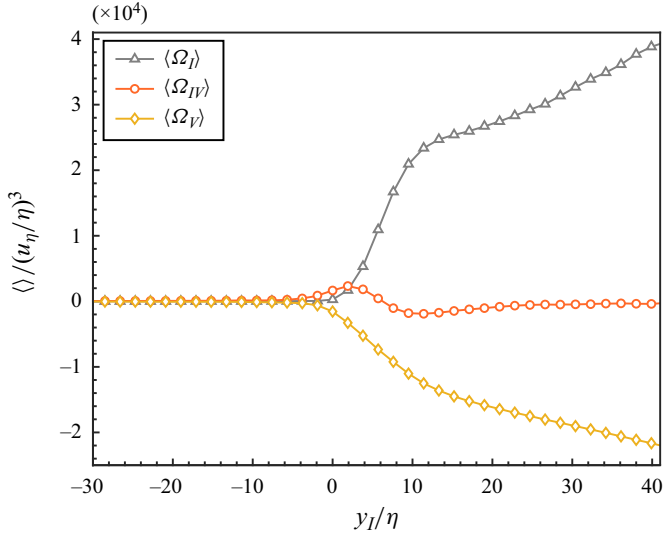
Figure 18. Conditional mean profiles of production, viscous diffusion and viscous dissipation.
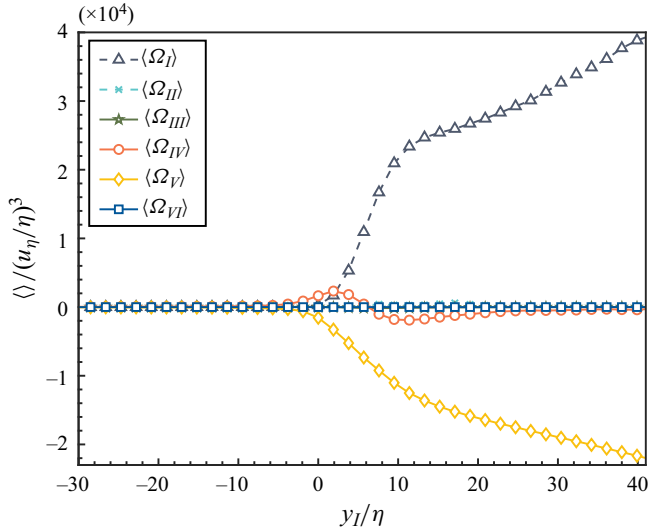

Figure 19. Conditional mean profiles of enstrophy transport components.

to decline rapidly at the interface coordinate 0 and then reached the minimum value of $-13.4\,\%$ at $y_I = 1.9\eta$. This suggests that compressibility tends to reduce the enstrophy of the turbulent fluids near the interface. After the minimum value, the proportion of the compressibility-related terms rapidly changes to a positive value with a maximum value of approximately $5.4\,\%$, indicating that the compressibility tends to increase the enstrophy of the fluids far away from the interface. After exceeding the interface thickness the contribution of compressibility is stable at approximately $1\,\%$–$2\,\%$.
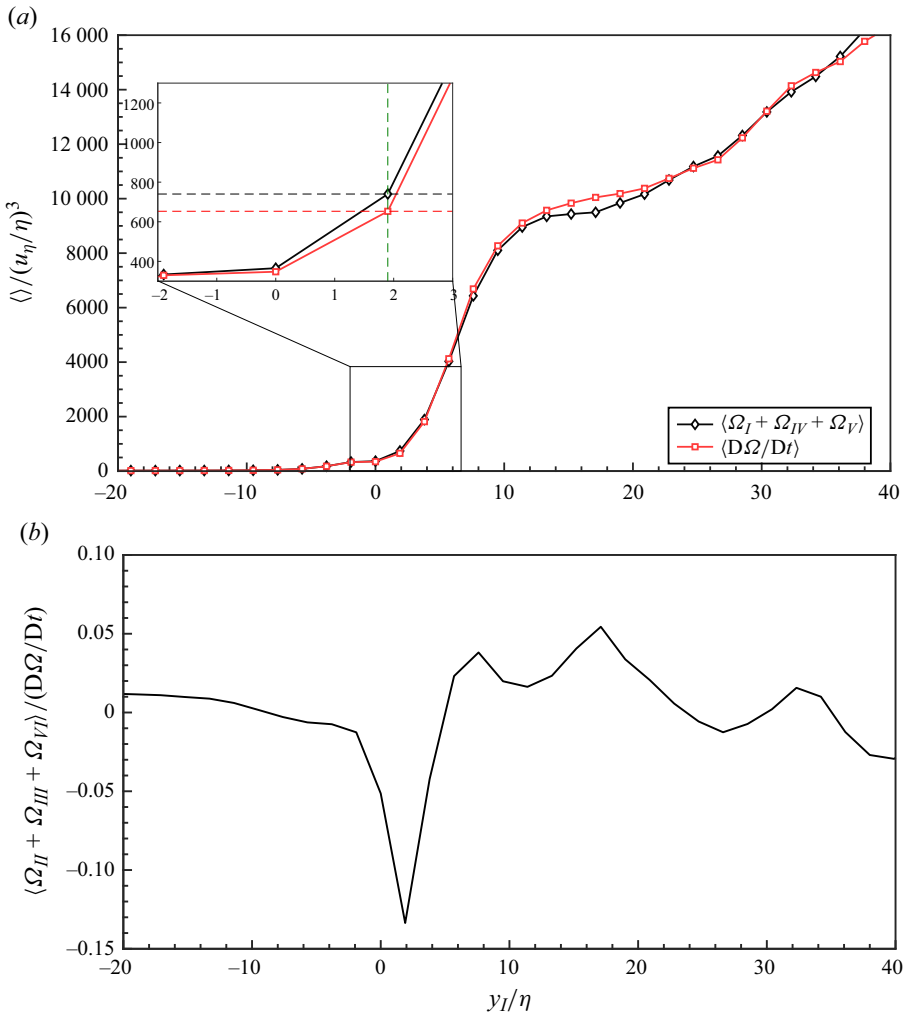
988 A30-20

(*a*)

(*b*)

Figure 20. The influence of compressibility. (*a*) Comparison of total enstrophy transportation and the contribution of compressibility irrelevant items. The changes near the interface are magnified. (*b*) Proportion of compressibility-related terms plotted against different locations in the interface coordinate system.

To make sure that the evaluation is reliable, the convergence of the result is investigated in figure 21. As the number of samples increases, the minimum percentage and its position in the interface coordinate become stable, which is -13% and $y_I = 1.9\eta$, respectively. This shows that compressibility tends to transfer the enstrophy of turbulence near the interface to both directions vertical to the interface, which promotes the expansion of the turbulent region to the non-turbulent region. This is also the reason why the mean height and the mean thickness of the interface are larger than those of the incompressible TBL (Corrsin & Kistler 1995; Wu *et al.* 2020) and compressible TBL with lower Mach number in the previous works (Zhang *et al.* 2018*b*).
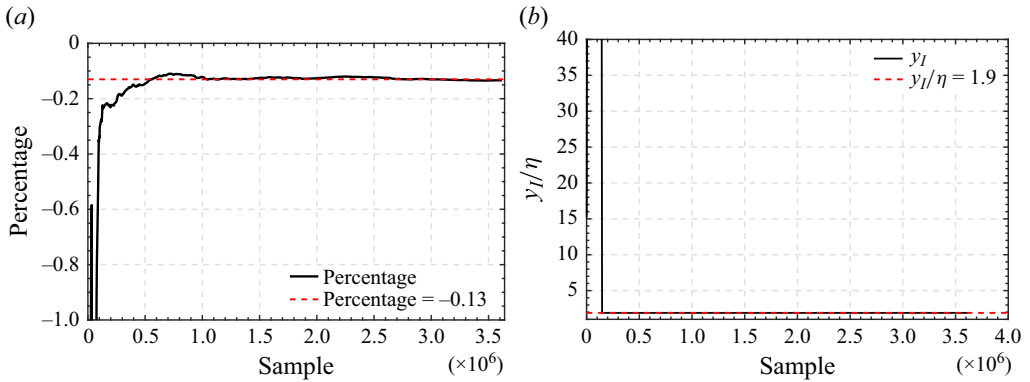
Figure 21. Convergence verification of compressibility effect. (*a*) The variation of minimum percentage plotted against the number of samples. (*b*) The position of the minimum percentage in the interface coordinate plotted against the number of samples.

4.2. *Entrainment characteristics*

From (4.8) and (4.3), the entrainment velocity of compressible flow can be calculated as follows:

$$
v_n = \frac{-2\omega_i\omega_j\dfrac{\partial u_i}{\partial x_j}}{|\nabla\Omega|} + \frac{2\Omega\dfrac{\partial u_j}{\partial x_j}}{|\nabla\Omega|} - \frac{\dfrac{2\omega_i\epsilon_{ijk}}{\rho^2}\dfrac{\partial\rho}{\partial x_j}\dfrac{\partial p}{\partial x_k}}{|\nabla\Omega|} - \frac{\nu\dfrac{\partial^2\Omega}{\partial x_j\partial x_j}}{|\nabla\Omega|}
$$
$$
+ \frac{2\nu\dfrac{\partial\omega_i}{\partial x_j}\dfrac{\partial\omega_i}{\partial x_j}}{|\nabla\Omega|} + \frac{\dfrac{2\omega_i\epsilon_{ijk}}{\rho^2}\dfrac{\partial\rho}{\partial x_j}\dfrac{\partial\tau_{km}}{\partial x_m}}{|\nabla\Omega|}. \tag{4.9}
$$

The p.d.f. of the entrainment velocity calculated from (4.9) is shown in figure 22(*a*). The p.d.f. deviates from the standard Gaussian distribution and has a negative skewness, which indicates that the turbulent region has a trend of outward expansion. The result is in good agreement with the previous results of incompressible TBL (Wolf *et al.* 2012; Mistry *et al.* 2019; Long *et al.* 2022) and compressible TBL (Zhang *et al.* 2018*b*). Figure 22(*b*) shows the p.d.f. of the contributions of different terms (v_{nI}–v_{nVI}, respectively) to the entrainment velocity, which is basically consistent with the previous result of the compressible flat TBL (Zhang *et al.* 2018*b*). The production term and viscous diffusion term have a large negative skewness, with the values of -3.04 and -2.83, respectively, while the skewness of the viscous dissipation term is positive, approximately 3.39. The skewness of the dilatation term and the baroclinic term is 0.38 and 0.34, respectively, which is smaller than compressibility independent terms. This indicates that the compressibility independent terms play a key role in the entrainment. Though the contribution of the compressibility-related term is small, it cannot be ignored.

Further statistical analysis shows that the average contribution of $-v_{nI}$–$-v_{nVI}$ (negative sign ensures positive entrainment when the mean value is positive) to the entrainment normalized by Kolmogorov velocity is approximately 0.22, 0.10, 0.01, 8.96, -7.99 and 0.0001, respectively; and the entrainment velocity is approximately 1.30 normalized by the Kolmogorov velocity. It can be seen that the mean contribution of the compressibility independent terms is relatively large and plays a key role in the entrainment. The mean entrainment velocity is increased by 8.5 % due to the contribution of compressibility.
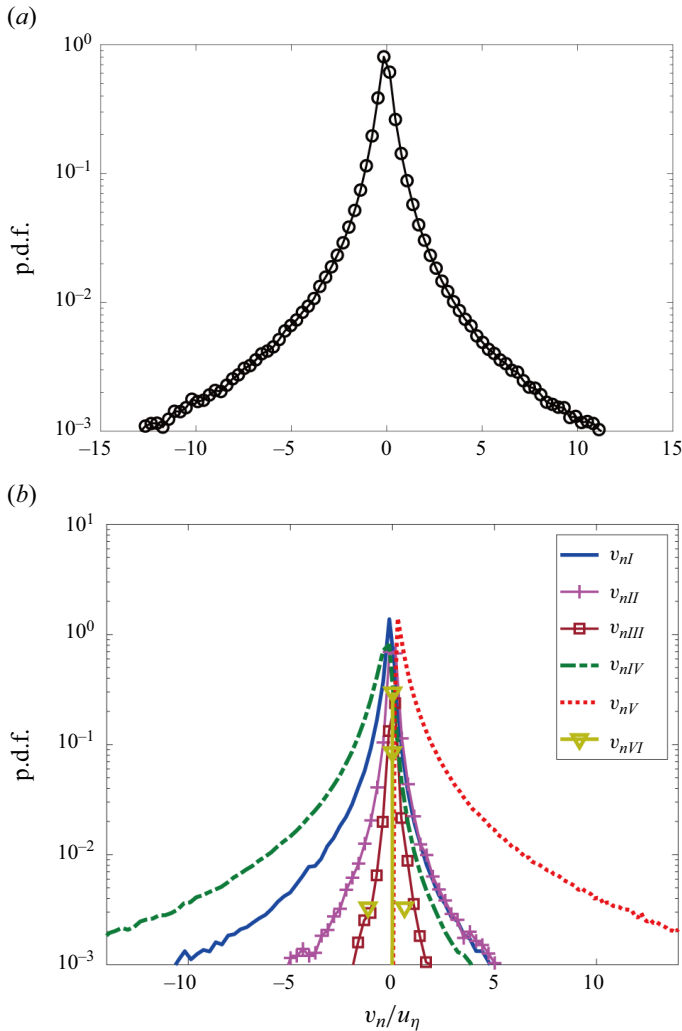
(*a*)

(*b*)

Figure 22. (*a*) Probability density function of entrainment velocity. (*b*) Probability density function of the contribution of different components to the entrainment velocity.

Based on the analysis of the p.d.f. and the mean value of entrainment velocity, it is shown that there may be a large deviation between instantaneous local entrainment velocity and its mean value. In order to explore the distribution law of instantaneous entrainment velocity, the relationship between local entrainment velocity and interface curvature is discussed according to the ideas of previous studies (Wolf *et al.* 2012, 2013; Jahanbakhshi & Madnia 2016; Mistry *et al.* 2019). In a two-dimensional interface, the curvature can be calculated by (4.10) (Mistry *et al.* 2019; Balamurugan *et al.* 2020), where *s* represents the length travelled along the interface curve starting from the starting point. Here *x* and *y* are the point coordinates on the interface, respectively. The positive curvature means that looking from the turbulent region, the interface has a concave surface towards the turbulent region; negative curvature means that the interface protrudes towards the non-turbulent region,
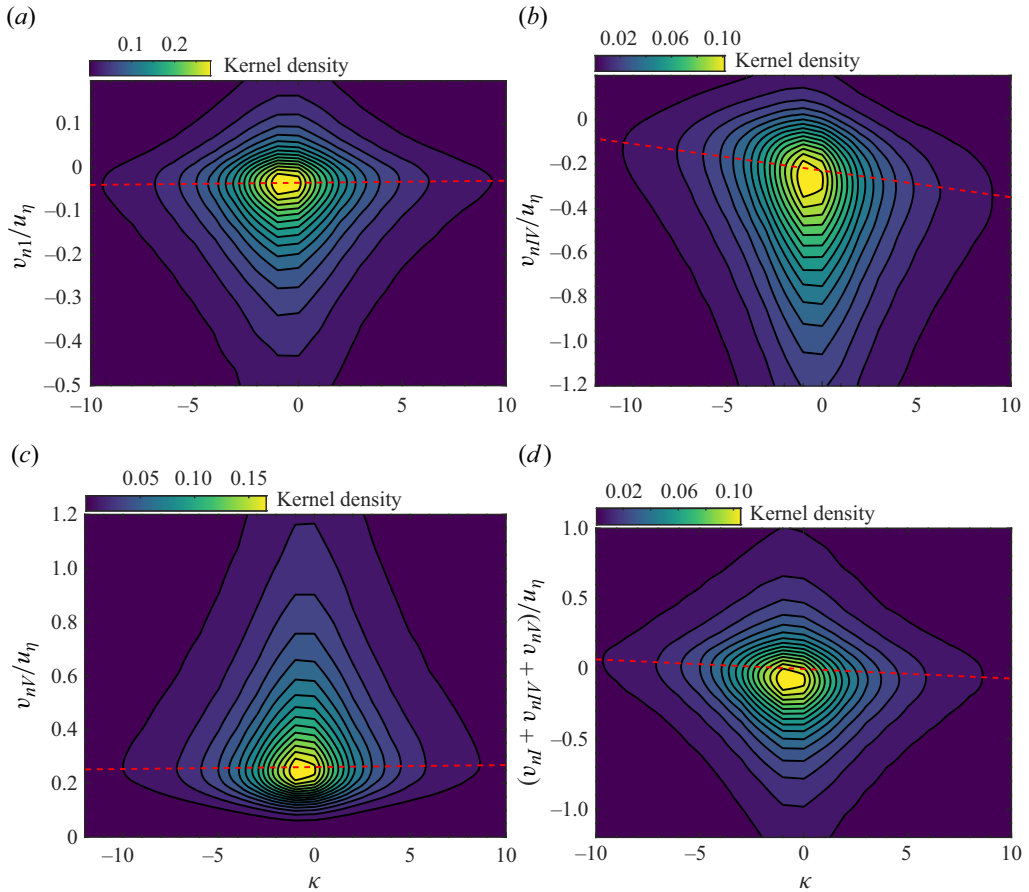
Figure 23. Joint p.d.f.s of local curvature and (*a*) production term, (*b*) viscous diffusion, (*c*) viscous dissipation, (*d*) compressibility independent term.

forming a convex surface:

$$\kappa = \frac{\dfrac{\mathrm{d}x}{\mathrm{d}s}\dfrac{\mathrm{d}^2 y}{\mathrm{d}s^2} - \dfrac{\mathrm{d}y}{\mathrm{d}s}\dfrac{\mathrm{d}^2 x}{\mathrm{d}s^2}}{\left[\left(\dfrac{\mathrm{d}x}{\mathrm{d}s}\right)^2 + \left(\dfrac{\mathrm{d}y}{\mathrm{d}s}\right)^2\right]^{3/2}}. \tag{4.10}$$

Figure 23(*a–c*) shows the joint p.d.f.s of the contribution of production term, viscous diffusion term and viscous dissipation term to the entrainment velocity and the local curvature of the interface. The red dotted line marks the ridge line of joint p.d.f., and the slope of the ridge line can be used to characterize the change of the contribution value with the local curvature. In figures 23(*a*) and 23(*c*), the ridge line is slightly tilted with a positive slope, indicating that as the local curvature of the interface increases, the contribution of the production term and viscous dissipation term to the entrainment decreases. In figure 23(*b*), the ridge line inclines more violently, and the slope is negative. This indicates that the contribution of the viscous diffusion term to the entrainment velocity has a significant increase with the increase of interface curvature. The total contribution of the
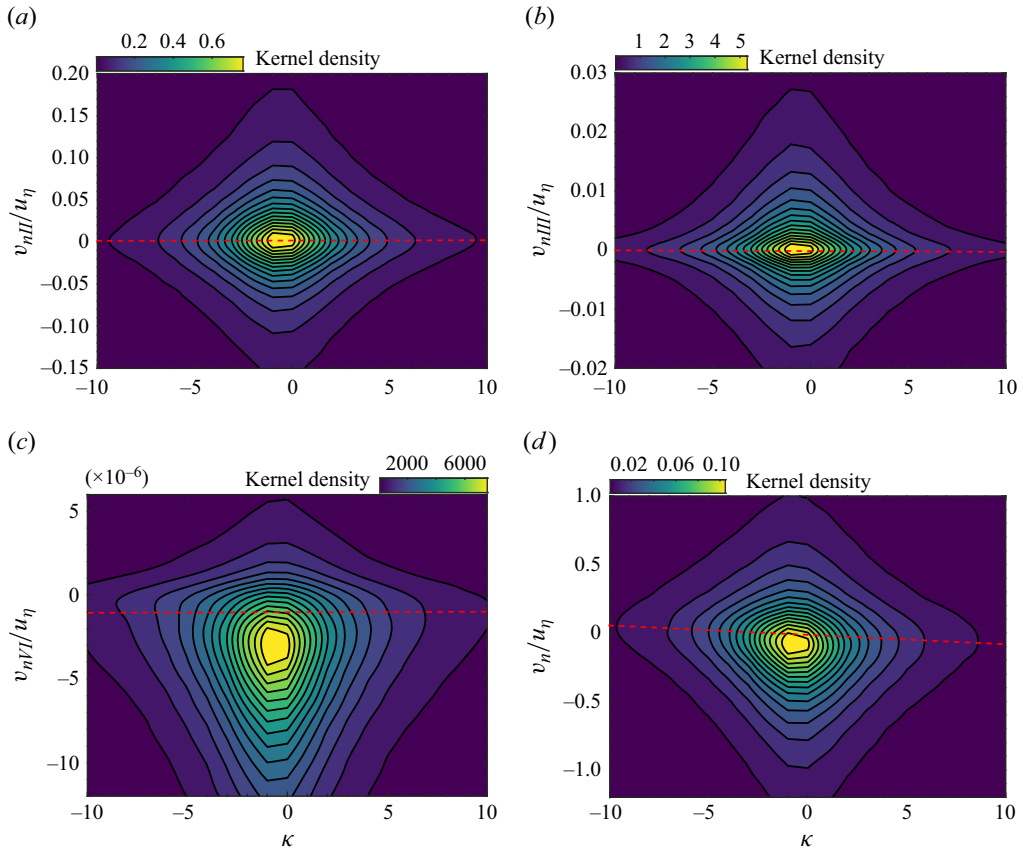
988 A30-24

Figure 24. Joint p.d.f.s of local curvature and (*a*) the dilatation term, (*b*) the baroclinic term, (*c*) the density gradient term, (*d*) the entrainment velocity.

compressibility independent terms composed of production term, viscous diffusion term and dissipation term to the entrainment velocity also shows a correlation with the interface curvature, as shown in figure 23(*d*).

For the terms related to compressibility, figure 24(*a*–*c*) shows the joint p.d.f.s of the contribution of (figure 24*a*) the dilatation term, (figure 24*b*) the baroclinic term, (figure 24*c*) the density gradient term and the local curvature of the interface. For these three terms, the ridge lines tend to be horizontal. This shows that the contribution of the compressibility-related terms to the entrainment velocity is basically independent of the local curvature of the interface. Figure 24(*d*) shows the joint density function of the entrainment velocity and local interface curvature. The ridge line is obviously inclined, and the slope is negative, indicating that the absolute value of the entrainment velocity is larger in the highly curved concave surface, while it is the opposite in the convex surface area. This suggests that the intense entrainment tends to occur near the highly curved concave surface of the interface (Wolf *et al.* 2012; Jahanbakhshi & Madnia 2016).

The influence of additional terms of enstrophy transport equation caused by compressibility on the interface entrainment is mainly analysed above, and the influence of compressibility on local entrainment mass flux will be further discussed in the following.
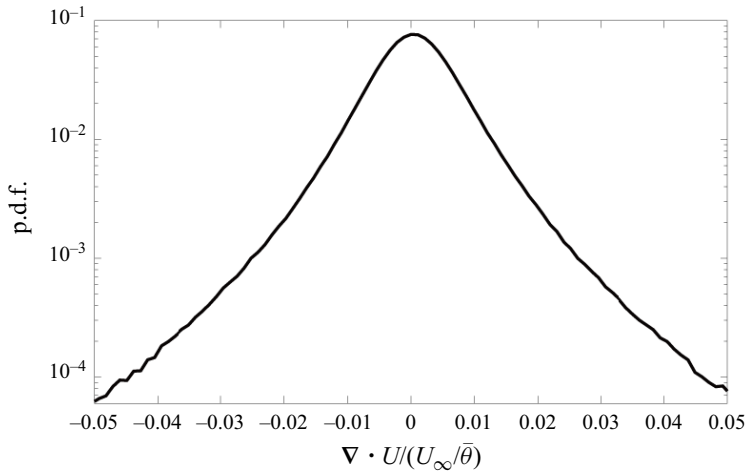
Figure 25. Probability density function of velocity divergence.

The compressibility of fluids is generally reflected in the expansion or compression of local volume, which can be quantitatively described by the dilatation, also known as the velocity divergence $\nabla \cdot U$. The p.d.f. of the velocity divergence is shown in figure 25. The peak value of the p.d.f. is located in the expansion area, and the probability of the expansion area on the TNTI is slightly greater than the probability of the compression area. In this work, the proportion of the expansion area is approximately 53.4 % of the interface.

The local entrainment mass flux can be determined by (Jahanbakhshi & Madnia 2016)

$$m = -\rho \cdot v_n, \tag{4.11}$$

and the negative sign is used to ensure that the mass flux is positive when the interface entrains.

The conditional mean profiles of the contribution of different terms in (4.8) to the entrainment mass flux conditioned on the divergence of the velocity are shown in figure 26, and the contribution of the production term slightly increases with the increase of velocity divergence. The dilatation term gradually decreases with the increase of velocity divergence. In the compression region, the dilatation term exhibits a positive effect, while in the expansion region the effect is negative. The viscous diffusion and dissipation term is relatively large in areas where the absolute value of divergence is not large. As the absolute value of divergence increases, the contribution of viscous diffusion and dissipation gradually decreases, indicating that the compression and expansion of the fluid have a certain hindrance effect on the viscosity at the interface. The baroclinic term and density gradient term are of small order of magnitude, and their effects on entrainment mass flux are not obvious. The hindrance effect of the compression and expansion of the fluids on the viscosity is not consistent in performance. For $-0.02 < \nabla \cdot U < 0$, as $\nabla \cdot U$ decreases, the contribution of viscous diffusion and dissipation to the entrainment flux gradually decreases. For $\nabla \cdot U < -0.02$, as the velocity divergence decreases, the contribution of viscosity to local entrainment flux remains basically unchanged. However, for $\nabla \cdot U > 0.01$, as the velocity divergence increases, the contribution of viscosity gradually decreases and the absolute value of the slope gradually increases, indicating that the expansion has a more significant hindrance effect on the viscosity at the interface. The
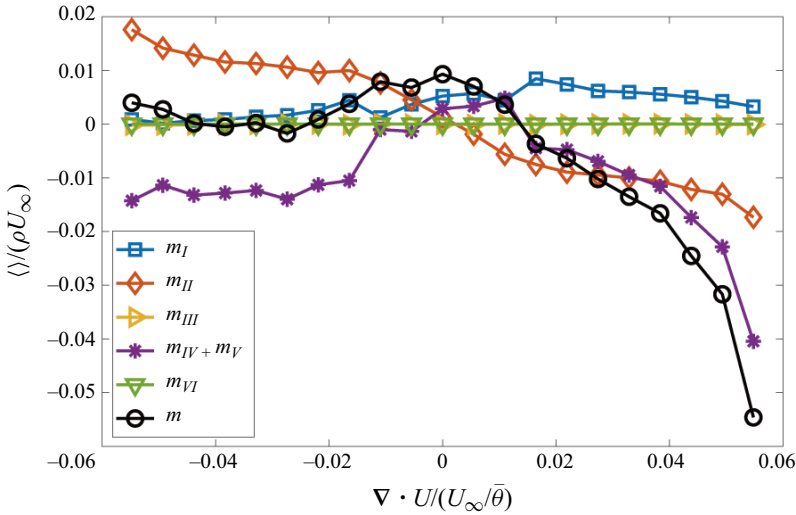
Figure 26. Local entrainment mass flux plotted against velocity divergence. Here $\bar{\theta}$ is the mean momentum thickness.

entrainment mass flux has a large positive value where the absolute value of divergence is small. With the increase of the absolute value of divergence, the hindrance effect reduces the contribution of viscosity to the entrainment flux, while the contribution of the dilatation term is opposite in the two regions. The superposition of the two makes the entrainment mass flux still positive in most of the compression regions and negative in the expansion regions. Therefore, interface entrainment is considered to mainly occur in areas with compression and slight expansion. The local entrainment mass flux is mainly dominated by the dilatation term, production term and viscosity terms, of which the dilatation term and production term have positive effects. The contribution of viscosity terms is positive only where the absolute value of divergence is small.

The mechanism of the hindrance effect of compressibility on viscous terms can be related to the behaviour of the dilatation term since it plays the biggest role in the part of compressible terms. The instantaneous contour plots of Ω_{II} and λ_{ci} have been shown in figure 27 to investigate the relationship between the dilatation term and local flow structures. It can be seen that the local maximum values of Ω_{II} are strongly associated with the vortex structures. More detailed distribution of Ω_{II} and the corresponding λ_{ci} fields near the interface has been provided in figure 28. As the dilatation term can be calculated as $\Omega_{II} = -2\Omega(\partial u_i/\partial x_i)$, the local maximum values should be strongly connected with the local maximum values of the enstrophy and λ_{ci} fields, and the plus or minus signs of the values are determined by the local flow state of compression or expansion. In the expansion area, the local minimum values of Ω_{II} appear while in the compression area the situation is the opposite. The expansion causes the enstrophy to diffuse outwards, making the interface develop from concave surface to convex surface and increasing the average height of the interface. The change in the geometry characteristic of the interface suppresses the viscous term, forming the hindrance effect. Some fluids may even pass through the interface forming detrainment, which corresponds to the results of m_{II} in figure 26. In the compression area, the convergence of the fluids enhances the entrainment process and forms a highly concave surface at the interface, which is conducive to the effect of viscous terms.
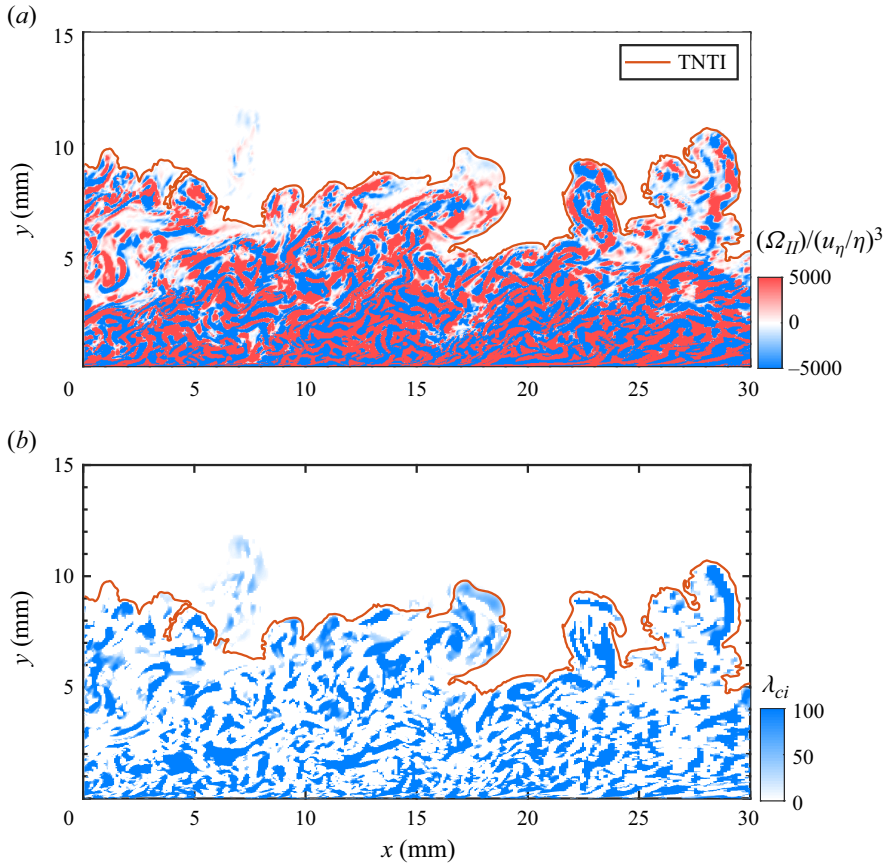
(*a*)

(*b*)

Figure 27. The instantaneous contour plots of dilatation terms Ω_{II} and λ_{ci}.

The local minimum and maximum values of Ω_{II} within the interface thickness range have been selected and the conditional mean profiles have been shown in figure 29. It can be observed that though the distributions show different tendencies along the coordinate, a local minimum value exists near the outer edge of the interface at $y_I \approx 2.5\eta$. This can be caused by the proportions of the expansion and compression area since the expansion area is larger than the compression area with a percentage of 53 %–54 %, which leads to the decrease in the total enstrophy transportation $D\Omega/Dt$.

A fact that needs to be elaborated on is that the conditional mean profiles of the dilatation term have a negative valley near the outer edge of the interface, which should have led to a negative contribution to the entrainment velocity. However, the dilatation term actually makes a positive contribution. This should be connected to the influence of the compressibility on the gradient of enstrophy $|\nabla\Omega|$. In the expansion area, the diffusion of enstrophy is enhanced, which increases the gradient of enstrophy $|\nabla\Omega|$. In the compression area, the diffusion of enstrophy is suppressed, and $|\nabla\Omega|$ also decreases. According to (4.3), the absolute values of the entrainment velocity contributed by the dilatation term in the compression region should be greater than the expansion area, which results in the conditional mean contribution to the entrainment velocity of the dilatation term remaining positive. The conditional mean profile of the $|\nabla\Omega|$ plotted against the dilatation term has been shown in figure 30. The symbol of the expansion pressure term represents the expansion and compression state of the fluid, with negative values
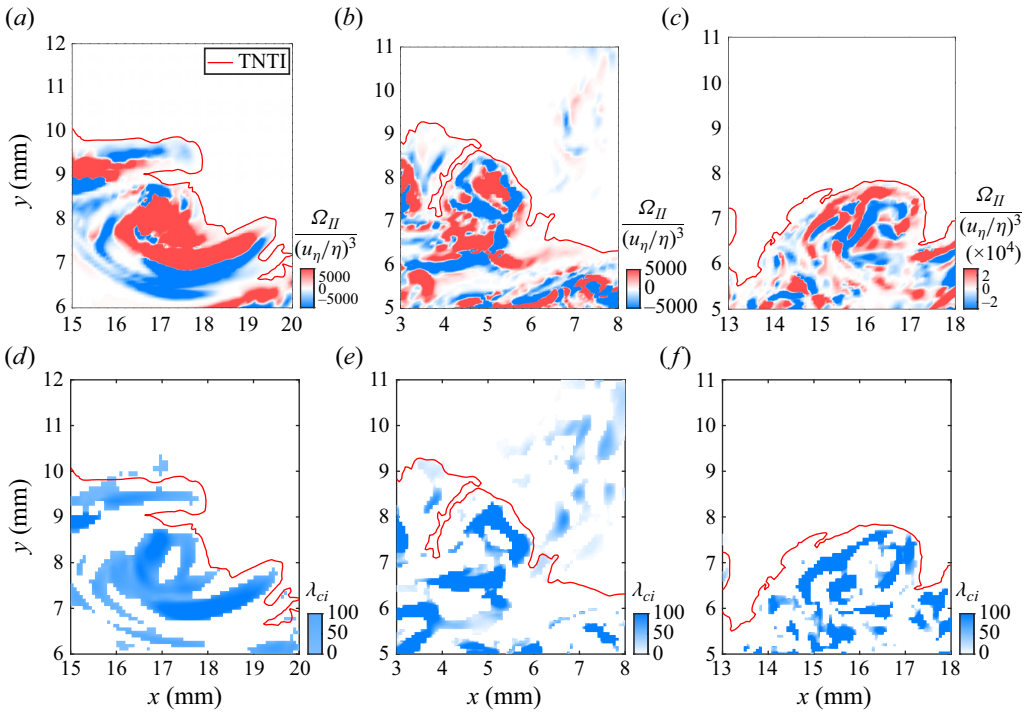
Figure 28. Local details of instantaneous contour plots of Ω_{II} and λ_{ci}.
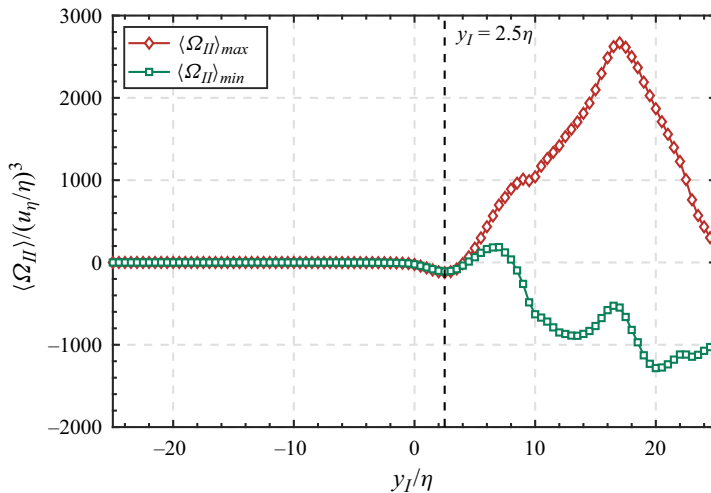

Figure 29. Conditional mean profiles of local minimum and maximum values of dilatation term.

indicating the expansion state and positive values indicating the compression state. It can be observed that in the case where the absolute values of the dilatation term are equal, $|\nabla\Omega|$ in the expansion area is greater than the compression area, which is consistent with the previous discussion. As the compressibility increases, the phenomenon may become more obvious. A lower $|\nabla\Omega|$ can also suppress the effect of viscous terms, that is why though compression is beneficial for the viscous terms, $m_{IV} + m_V$ is still negative in the compression area.
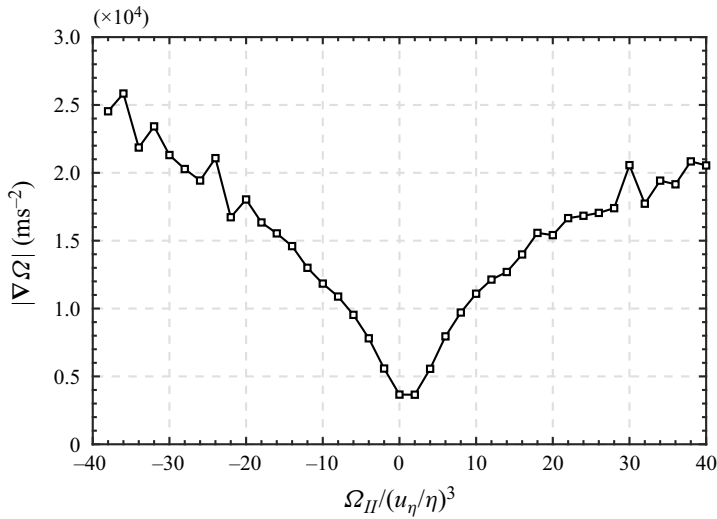
Figure 30. The conditional mean profile of the $|\nabla\Omega|$ plotted against the dilatation term.

5. Conclusion

The influence of compressibility on the geometric features and the entrainment characteristics of the interface is mainly discussed with Mach 2.9 and the main conclusions drawn in this paper are as follows.

Based on the DNS results, it is found that the flow can form a fully developed compressible TBL. In the turbulent region, the mean and r.m.s. height, the average thickness of the interface and the fractal dimension are obtained. It is found that compressibility tends to increase the height and the thickness of the interface.

The components of enstrophy transport generated by compressibility independent terms are in the same order of magnitude near the interface, and play a key role in the enstrophy transportation. The dilatation term, baroclinic term and density gradient term generated by compressibility are of smaller order of magnitude, but the total net effect of the three terms is relatively obvious, accounting for up to 13.4 % of the enstrophy transportation, and tends to transfer the enstrophy of turbulence near the interface to both directions vertical to the interface, which promotes the expansion of the turbulent region to the non-turbulent region. Therefore, the mean height, thickness and entrainment velocity of the interface are increased by 3.7 %, 7.0 % and 8.5 %, respectively, due to the compressibility.

The contribution of the compressibility-related terms to the entrainment velocity is basically independent of the local curvature of the interface, while the viscous diffusion term shows a strong correlation with the local curvature of the interface, which indicates that the intense entrainment process tends to occur at the highly curled concave surface of the interface.

The entrainment on the interface mainly occurs in the compression region and the expansion region with small velocity divergence. The dilatation term is one of the main contributors to the entrainment mass flux in the interface compression region. Both the compression and expansion of the interface will have a certain hindrance effect on the viscosity, of which the hindrance effect of expansion is more significant. At the same time, the dilatation term's contribution is negative in the expansion area of the interface, which leads to a significant reduction in the local entrainment mass flux in the expansion area.

The hindrance effect of the compressibility is related to the behaviour of the dilatation term. The dilatation term is associated with the vortex structures and the local flow state of compression or expansion. The expansion causes the enstrophy to diffuse outwards, making the interface develop from a concave surface to a convex surface and increasing the average height of the interface while the compression leads to the opposite. The change in the interface shape forms the hindrance effect on the viscous term. The percentage of the expansion area is slightly higher than the compression area, which reduces the total enstrophy transportation near the interface. The gradient of enstrophy is also affected by the compressibility and it is greater in the expansion area. The lower $|\nabla \Omega|$ in the compression area also suppresses the viscous terms, which results in the hindrance effect in the compression area.

Declaration of interests. The authors report no conflict of interest.

Author ORCIDs.

- Shuhuai Su https://orcid.org/0009-0007-0481-5599;
- Yanguang Long https://orcid.org/0000-0002-8201-9308;
- Jinjun Wang https://orcid.org/0000-0001-9523-7403;
- Xinliang Li https://orcid.org/0000-0002-4264-9620.

REFERENCES

AGUIRRE, R.C. & CATRAKIS, H.J. 2020 On intermittency and the physical thickness of turbulent fluid interfaces. *J. Fluid Mech.* **540** (1), 39.

BALAMURUGAN, G., RODDA, A., PHILIP, J. & MANDAL, A.C. 2020 Characteristics of the turbulent non-turbulent interface in a spatially evolving turbulent mixing layer. *J. Fluid Mech.* **894**, A4.

BORRELL, G. & JIMENEZ, J. 2016 Properties of the turbulent/non-turbulent interface in boundary layers. *J. Fluid Mech.* **801**, 554–596.

CHAUHAN, K., PHILIP, J., DE SILVA, C.M., HUTCHINS, N. & MARUSIC, I. 2014 The turbulent/non-turbulent interface and entrainment in a boundary layer. *J. Fluid Mech.* **742**, 119–151.

COGO, M., SALVADORE, F., PICANO, F. & BERNARDINI, M. 2022 Direct numerical simulation of supersonic and hypersonic turbulent boundary layers at moderate-high Reynolds numbers and isothermal wall condition. *J. Fluid Mech.* **945**, A30.

CORRSIN, S. & KISTLER, A.L. 1995 Free-stream boundaries of turbulent flows. *NACA Tech. Rep.* TN-1244.

DAHM, W.J.A. & DIMOTAKIS, P.E. 1987 Measurements of entrainment and mixing in turbulent jets. *AIAA J.* **25** (9), 1216–1223.

DANG, G, LIU, S., DUAN, J. & LI, X 2022 Direct numerical simulation of compressible turbulence accelerated by graphics processing unit: an open-access database of high-resolution direct numerical simulation. *AIP Adv.* **12** (12), 125111.

DIMOTAKIS, P.E. 2000 The mixing transition in turbulent flows. *J. Fluid Mech.* **409**, 69–98.

DUAN, J., LI, X., LI, X. & LIU, H. 2021 Direct numerical simulation of a supersonic turbulent boundary layer over a compression–decompression corner. *Phys. Fluids* **33** (6), 065111.

DUAN, L., BEEKMAN, I. & MARTÍN, M.P. 2011 Direct numerical simulation of hypersonic turbulent boundary layers. . *J. Fluid Mech.* **672**, 245–267.

EISMA, J., WESTERWEEL, J., OOMS, G. & ELSINGA, G.E. 2015 Interfaces and internal layers in a turbulent boundary layer. *Phys. Fluids* **27** (5), 055103.

FERRÉ, J., MUMFORD, J., SAVILL, A. & GIRALT, F. 1990 Measurements of entrainment and mixing in turbulent jets. *J. Fluid Mech.* **210**, 371–414.

GAMPERT, M., KLEINHEINZ, K., PETERS, N. & PITSCH, H. 2014 Experimental and numerical study of the scalar turbulent/non-turbulent interface layer in a jet flow. *Flow Turbul. Combust.* **92** (1–2), 429–449.

HOLZNER, M. & LÜTHI, B. 2011 Laminar superlayer at the turbulence boundary. *Phys. Rev. Lett* **106** (13), 134503.

JAHANBAKHSHI, R. & MADNIA, C.K. 2016 Entrainment in a compressible turbulent shear layer. *J. Fluid Mech.* **797**, 564–603.

LEE, J., SUNG, H.J. & ZAKI, T.A. 2017 Signature of large-scale motions on turbulent/non-turbulent interface in boundary layers. *J. Fluid Mech.* **819**, 165–187.

LONG, Y., WANG, J. & PAN, C. 2022 Universal modulations of large-scale motions on entrainment of turbulent boundary layers. *J. Fluid Mech.* **941**, A68.

LONG, Y., WU, D. & WANG, J. 2021 A novel and robust method for the turbulent/non-turbulent interface detection. *Exp. Fluids* **62** (7), 138.

MARTÍN, M.P., TAYLOR, E.M., WU, M. & WEIRS, V.G. 2006 A bandwidth-optimized weno scheme for the effective direct numerical simulation of compressible turbulence. *J. Comput. Phys.* **220** (1), 270–289.

MATHEW, J. & BASU, A.J. 2002 Some characteristics of entrainment at a cylindrical turbulence boundary. *Phys. Fluids* **14** (7), 2065.

MISTRY, D., PHILIP, J. & DAWSON, J.R. 2019 Kinematics of local entrainment and detrainment in a turbulent jet. *J. Fluid Mech.* **871**, 896–924.

MUNGAL, M.G., KARASSO, P.S. & LOZANO, A. 1991 The visible structure of turbulent jet diffusion flames: large-scale organization and flame tip oscillation. *Combust. Sci. Technol.* **76** (4–6), 165–185.

NATRAJAN, V.K. & CHRISTENSEN, K.T. 2006 The role of coherent structures in subgrid-scale energy transfer within the log layer of wall turbulence. *Phys. Fluids* **18** (6), 065104.

OSAKA, H., KAMEDA, T. & MOCHIZUKI, S. 1998 Re-examination of the Reynolds-number-effect on the mean flow quantities in a smooth wall turbulent boundary layer. *JSME Intl J.* B **41** (1), 123–129.

PHILIP, J., BERMEJO-MORENO, I., CHUNG, D. & MARUSIC, I. 2015 Characteristics of the entrainment velocity in a developing wake. In *Proceedings of the Ninth International Symposium on Turbulence and Shear Flow Phenomena (TSFP-9), Melbourne, Australia*, vol. 3, paper 9C-5.

PIROZZOLI, S., GRASSO, F. & GATSKI, T.B. 2004 Direct numerical simulation and analysis of a spatially evolving supersonic turbulent boundary layer at $m = 2.25$. *Phys. Fluids* **16** (3), 530–545.

PRASAD, R.R. & SREENIVASAN, K.R. 1989 Scalar interfaces in digital images of turbulent flows. *Exp. Fluids* **7**, 259–264.

QIAN, Y. 2004 *Aerodynamics*. Beihang University Press.

SCHLICHTING, H. & GERSTEN, K. 2017 *Boundary-Layer Theory*. Springer.

DA SILVA, C.B., HUNT, J.C.R., EAMES, I. & WESTERWEEL, J. 2014 Interfacial layers between regions of different turbulence intensity. *Annu. Rev. Fluid Mech.* **46** (1), 567–590.

DE SILVA, C.M., PHILIP, J., CHAUHAN, K., MENEVEAU, C. & MARUSIC, I. 2013 Multiscale geometry and scaling of the turbulent-nonturbulent interface in high Reynolds number boundary layers. *Phys. Rev. Lett.* **111** (4), 044501.

VAN DRIEST, E.R. 1951 Turbulent boundary layer in compressible fluids. *J. Aeronaut. Sci.* **18** (3), 145–160.

WATANABE, T., NAITO, T., SAKAI, Y., NAGATA, K. & ITO, Y. 2015 Mixing and chemical reaction at high Schmidt number near turbulent/nonturbulent interface in planar liquid jet. *Phys. Fluids* **27** (3), 035114.

WATANABE, T., ZHANG, X. & NAGATA, K. 2018 Turbulent/non-turbulent interfaces detected in DNS of incompressible turbulent boundary layers. *Phys. Fluids* **30** (3), 035102.

WOLF, M., HOLZNER, M., LÜTHI, B., KRUG, D., KINZELBACH, W. & TSINOBER, A. 2013 Effects of mean shear on the local turbulent entrainment process. *J. Fluid Mech.* **731**, 95–116.

WOLF, M., LÜTHI, B., HOLZNER, M., KRUG, D., KINZELBACH, W. & TSINOBER, A. 2012 Investigations on the local entrainment velocity in a turbulent jet. *Phys. Fluids* **24** (10), 105110.

WU, D., WANG, J., CUI, G. & PAN, C. 2020 Effects of surface shapes on properties of turbulent/non-turbulent interface in turbulent boundary layers. *Sci. China Technol. Sci.* **63** (2), 214–222.

XU, D., WANG, J. & CHEN, S. 2023 Reynolds number and wall cooling effects on correlations between the thermodynamic variables in hypersonic turbulent boundary layers. *J. Fluid Mech.* **965**, A4.

ZHANG, C., DUAN, L. & CHOUDHARI, M.M. 2018*a* Direct numerical simulation database for supersonic and hypersonic turbulent boundary layers. *AIAA J.* **56** (11), 4297–4311.

ZHANG, X., WATANABE, T. & NAGATA, K. 2018*b* Turbulent/nonturbulent interfaces in high-resolution direct numerical simulation of temporally evolving compressible turbulent boundary layers. *Phys. Rev. Fluids* **3** (9), 094605.

ZHANG, X., WATANABE, T. & NAGATA, K. 2023 Reynolds number dependence of the turbulent/non-turbulent interface in temporally developing turbulent boundary layers. *J. Fluid Mech.* **964**, A8.

ZHUANG, Y., TAN, H., HUANG, H., LIU, Y. & ZHANG, Y. 2018 Fractal characteristics of turbulent–non-turbulent interface in supersonic turbulent boundary layers. *J. Fluid Mech.* **843**, R2.